Article

Not peer-reviewed version

Corrosion Resistance of the Welded Joints From the Ultrafine-Grained Near-α Titanium Alloys Ti-5Al-2V Obtained by Spark Plasma Sintering

V. N. Chuvil'deev , A. V. Nokhrin * , C. V. Likhnitskii , V. I. Kopylov , P. V. Andreev , M. S. Boldin , N. Yu. Tabachkova , A. I. Malkin

Posted Date: 27 January 2023

doi: 10.20944/preprints202301.0501.v1

Keywords: titanium alloy; ultrafine-grained microstructure; equal channel angular pressing; spark plasma sintering; diffusion welding; corrosion; hat salt corrosion; diffusion; grain boundary.

Article

Corrosion Resistance of the Welded Joints from the Ultrafine-Grained Near-α Titanium Alloys Ti-5Al-2V Obtained by Spark Plasma Sintering

V.N. Chuvil'deev [1], A.V. Nokhrin [1,*], C.V. Likhnitskii [1], V.I. Kopylov [1], P.V. Andreev [1], M.S. Boldin [1], N.Yu. Tabachkova [2,3] and A.I. Malkin [4]

[1] Materials Science Department, Physical and Technical Research Institute, Lobachevsky State University of Nizhny Novgorod, 603022, Nizhny Novgorod, Russia; chuvildeev@nifti.unn.ru (V.N.C.); likhnitskiy@nifti.unn.ru (C.V.L.); kopylov@nifti.unn.ru (V.I.K.); andreev@phys.unn.ru (P.V.A.); boldin@nifti.unn.ru (M.S.B.)

[2] Center Collective Use "Materials Science and Metallurgy", National University of Science and Technology "MISIS", 119991, Moscow, Russia; ntabachkova@misis.ru (N.Y.T.)

[3] Laboratory "FIANIT", Laser Materials and Technology Research Center, A.M. Prokhorov General Physics Institute of the Russian Academy of Sciences, 119991, Moscow, Russia; ntabachkova@gmail.com (N.Y.T.)

[4] Laboratory of Physico-Chemical Mechanics and Mechanochemistry, A.N. Frumkin Institute of Physical Chemistry and Electrochemistry, Russian Academy of Science, 119071, Moscow, Russia; mlkn@list.ru (A.I.M.)

* Correspondence: nokhrin@nifti.unn.ru (A.V.N.)

Abstract: A diffusion welding of coarse-grained and ultrafine-grained (UFG) specimens of titanium near-α alloy Ti-5Al-2V used in nuclear power engineering was made by Spark Plasma Sintering. The failure of the welded specimens in the conditions of hot salt corrosion and of electrochemical corrosion were shown to have preferentially intercrystalline character. In the case of presence of macrodefects, crevice corrosion of the welded joints was observed. The resistance of the alloys against the intercrystalline corrosion was found to be determined by the concentration of vanadium at the titanium grain boundaries, by the size and volume fraction of the β-phase particles and by the presence of micro- and macropores in the welded joints. The specimens of the welded joints of the UFG alloy have higher hardness, hot salt corrosion resistance and the electrochemical corrosion.

Keywords: titanium alloy; ultrafine-grained microstructure; equal channel angular pressing; spark plasma sintering; diffusion welding; corrosion; hat salt corrosion; diffusion; grain boundary

1. Introduction

At present, titanium α- and near-α alloys (alloys of Ti-Al-V, Ti-Al-Zr, Ti-Al-Mo-V, etc. systems) are used widely in marine engineering, steam turbines, nuclear power engineering, etc. [1–7]. Enhanced requirements of strength, ductility, fatigue strength, corrosion and radiation resistance, heat resistance, etc. are imposed onto the titanium alloys used in nuclear power engineering [3–11].

Traditionally, the enhancement of the mechanical properties and of the performance characteristics of the titanium alloys are provided by means of optimization of their chemical composition as well as by choice of regimes of thermal and deformation treatments [1–6,8,10]. Formation of an ultrafine-grained (UFG) microstructure of the titanium alloys using the severe plastic deformation (SPD) methods is one of promising methods of increasing the performance characteristics of these ones. The Equal Channel Angular Pressing (ECAP) [12,13], High Pressure Torsion [14,15], Rotary Swaging [16,17], Multiaxial Forging/Pressing [18,19], etc. are used to form the UFG microstructure in the Ti alloys most often. The UFG titanium alloys obtained by SPD, are featured by enhanced strength [14,16–19], fatigue resistance [20–22], creep resistance [23,24], corrosion resistance [25,26], ductility at high temperature [19,24,27], etc. This allows fabricating lighter, stronger, and more reliable structural elements from the UFG titanium alloys.

 doi:10.20944/preprints202301.0501.v1

From the viewpoint of application of the Ti alloys in Nuclear Engineering, the opportunity to ensure the strength and corrosion resistance by means of the use of SPD is important. At present, the forming of the UFG microstructure is commonly accepted to result in an increased strength of the Ti alloys in most cases [12–14,17–19]. The issue of high corrosion resistance of the UFG Ti and α-Ti alloys is still ambiguous. Most publications demonstrated UFG Ti to have a higher corrosion resistance because of forming denser and thicker native oxide surface layers [25,28–31]. However, there are some works where the opposite results were reported evidencing the reduction of the corrosion resistance of UFG Ti [32–34]. It was also noted in [34] that texture formation during SPD has a greater influence on the corrosion resistance of titanium than grain size. In [35,36], it was shown that an increasing of the oxygen concentration in the surface layers of Ti may occur at SPD whereas a hydrogenation of the UFG Ti surface takes place at long exposure to an acid ambient. This may lead to a change in the corrosion rate in acids – at short testing times, UFG Ti may possesses a lower corrosion rate as compared to the coarse-grained specimens whereas at long times – the corrosion rate may increase considerably and exceed the corrosion rate of coarse-grained Ti [36].

A problem of developing a technology of welding the UFG titanium alloys is an important one limiting their wide application. At present, argon arc beam or electron beam technologies of welding the titanium alloys are used for the fabrication of the long workpieces in the nuclear industry most often [3,37–40]. The welding of specimens using these technologies is associated by the melting of the welded joint region and, hence, does not allow preserving the UFG microstructure in the welded joint. Such novel technologies of solid-phase welding as linear friction welding or friction-stir welding [41–43] have not got wide application yet due to essential and uncontrolled overheating of the welding zone and pollution of the joint region by external impurities from the processing tool (punch) material. These features of conventional welding technologies result in poor performance characteristics of the welded joints (in particular, of the corrosion resistance [44]) and, hence, may limit the operational reliability and durability of highly responsible metal microstructures.

Spark Plasma Sintering (SPS) [45–47] is one of novel promising methods of the solid-phase welding and bonding of the structural materials, including titanium alloys [48,49]. The efficiency of application of this method for diffusion welding / bonding of the titanium alloys has been demonstrated recently in [50,51]. An opportunity to control and monitor the temperature and time of the diffusion welding, heating rate, and applied pressure, to apply step-wise heating regimes with simultaneous monitoring the shrinkage of the specimens in the course of welding or sintering directly is an important advantage of SPS [50,51]. An opportunity to implement high heating rates (up to 2500 ^{o}C/min) allows minimizing the grain growth and, hence, allows preserving the fine-grained microstructure with enhanced performance characteristics in the welded joints. Earlier, SPS was shown to allow high-speed diffusion welding of UFG near-α Ti alloys Ti-5Al-2V [51]. High heating rates allowed preserving the fine grains in the UFG Ti-5Al-2V alloy that allowed reducing the diffusion mass transfer scale and, hence, improving the solid phase diffusion welding intensity at reduced temperatures [51]. The application of SPS to ensure the high operational characteristics of the welded joints in Ti alloys may also be very promising because of a positive effect of pulsed electric current on the mechanical properties of the Ti-Al-V alloys discovered recently [52]. Note also that SPS technology allows obtaining the powder titanium alloys with high mechanical properties and high corrosion resistance (see Table 1 in [53]).

A problem of providing high strength and corrosion resistance of the welded joints of the near-α Ti alloys by joint application of SPD and SPS is of special interest. From the viewpoint of application of the UFG near-α Ti alloys in nuclear engineering, providing a high resistance of these ones to hot salt corrosion (HSC) is especially important.

HSC results in a severe degradation of the heat-exchange equipment of produced from the titanium α- and near-α alloys [3,8,10,54–56]. The HSC of the titanium alloys has a complex nature and is a multistage process of fracture, in which the chemical and electrochemical destruction in the conditions of action of elevated temperatures, corrosion-aggressive ambient, aces of oxygen as well as (in some cases) of the action of tensile strain are alternating sequentially [54–56]. HSC arises at the forming of porous deposits from the hard salts on the surface of the heat exchangers made from Ti

Preprints (www.preprints.org) | NOT PEER-REVIEWED | Posted: 27 January 2023 doi:10.20944/preprints202301.0501.v1

alloys at elevated temperatures followed by concentration of corrosion-aggressive components insolvable in water (chlorides and bromides of alkaline and alkaline earth materials) in these ones [54–56]. As it was noted in [54–56], HSC goes most intensively at direct contact of Ti alloys with crystalline halide salts (chlorides, bromides, iodides), in the presence of water (bound in crystal hydrates, occluded in salt crystals, or present in ambient air), and with air access This leads to the forming of corrosion products on the surfaces of the Ti alloys in the form of layers of varied composition [54,57]. The size and composition of these layers depend on the alloy composition and on the testing regime. Some authors noted the Ti alloys containing Al to be most susceptible to HSC [58]. At present, most studies on HSC of Ti alloys is concentrated on a problem of stress corrosion cracking of high-strength two-phase Ti alloys for aircraft industry [59–61]. Less attention is paid to a problem of HSC in α- and near-α Ti alloys used in nuclear engineering at lower stresses and temperatures. We have found no works devoted to a problem of HSC of welded joints of UFG Ti alloys obtained by SPS. In the present work, the features of corrosion destruction of the welded joints in the UFG near-α Ti alloys was analyzed for the first time. First results on studying the resistance of the powder titanium alloys obtained by SPS in the HSC conditions were presented in [53].

Note that a positive effect of high-temperature SPD on the resistance of near-α Ti alloys to HSC was reported earlier [26]. This allows expecting joint application of SPD and SPS to allow ensuring a high resistance of the welded joints against HSC.

The present work was aimed at studying the features of destruction of the welded joints of the titanium near-α alloy specimens in the HSC conditions and, in particular, studying the effect of microstructure parameters and SPS modes of the welded titanium near-α alloy specimens on the resistance to the HSC.

2. Materials and Methods

The study focuses on Ti-4.73wt.%Al-1.88wt.%V alloy (Russian industrial alloy PT-3V). The PT-3V alloy is an analog of Grade 9 alloy (Ti – (2.5-3.5)%Al-(2-3)%V) but differs from this one by an increased Al content. The bars of alloy of 20 mm in diameter were made by Chepetsky Mechanical Plant Co. by hot deformation with gradual reduction of temperature from the β-phase range to the (α+β)-one (see [62–64]). The chemical composition of the alloy is presented in Table 1. The chemical composition of the alloy meets the requirements of Russian National Standard GOST 19807-91. This alloy is one of near-α titanium alloys, the volume ratio of β-phase in which does not exceed 5%. General chemical analysis of the alloy is carried out using FOUNDRY®-Master™ spectrum analyzer. The concentrations of oxygen, nitrogen, carbon, and hydrogen were measured by reductive melting using ELTRA® ON-900 (control over O_2, C, N_2) and ELTRA® OH-900 (control over H_2) analyzers.

Table 1. Compositions of the titanium alloy PT-3V.

	Contents of alloying elements, wt.%									
	Ti	**Al**	**V**	**Zr**	**Fe**	**Si**	**O**	**N**	**C**	**H**
Tested alloy	Balance	4.73	1.88	0.019	0.11	0.03	0.042	0.01	0.0024	0.004
Russian standard GOST 19807-91	Balance	3.5-5.0	1.2-2.5	≤0.30	≤0.25	≤0.12	≤0.15	≤0.04	≤0.1	≤0.006

The UFG microstructure in the alloy was formed with ECAP in the B_c route (the number of the ECAP cycles N=4, the ECAP temperature was 450 °C, the ECAP rate was 0.2-0.4 mm/s). ECAP was performed with Ficep® HF400L hydraulic press. Before pressing, the specimens of 14×14×140 mm in size were held in the operating channel of the ECAP setup for 10 min. The accuracy of temperature control during ECAP was ± 10 °C.

The diffusion welding of specimens of 7×7×3.5 mm in size was performed using Dr. Sinter® SPS-625 setup. The specimens for investigations were obtained by spark cutting into pieces of 14×14×140 mm in size. Surface roughness varied as a result of polishing with diamond paste of different dispersion level. The surface roughness in specimens was 40 to 60 μm.

Preprints (www.preprints.org) | NOT PEER-REVIEWED | Posted: 27 January 2023 doi:10.20944/preprints202301.0501.v1

The heating rate V_h varied from 10 to 350 °C/min, the applied uniaxial stress P changed from 50 to 100 MPa, the processing time varied from 0 to 90 min. The welding temperature T ranged from 600 to 1140 °C: the welding was performed in the α-region (T = 600 °C), near the boundary of the α-β phase transition for the Ti-Al-V alloys (T = 700 °C), in the beginning of the two-phase α+βregion (T = 800 °C), and in the region of stable β-phase (T = 1030, 1140 °C) (see [62–64]). The accuracy of temperature control was ± 10 °C. Welding was performed in vacuum (6 Pa). The diffusion welding of the flat specimens was performed in a free state without the use of the graphite molds (Figure 1a) limiting the expansion process at the plastic deformation of the material in the radial direction. It leads to the formation of the tangent strain acting along the axis of the specimen junction (normal to the axis of the uniaxial stress P = 50, 70, 100 MPa) (Figure 1b).

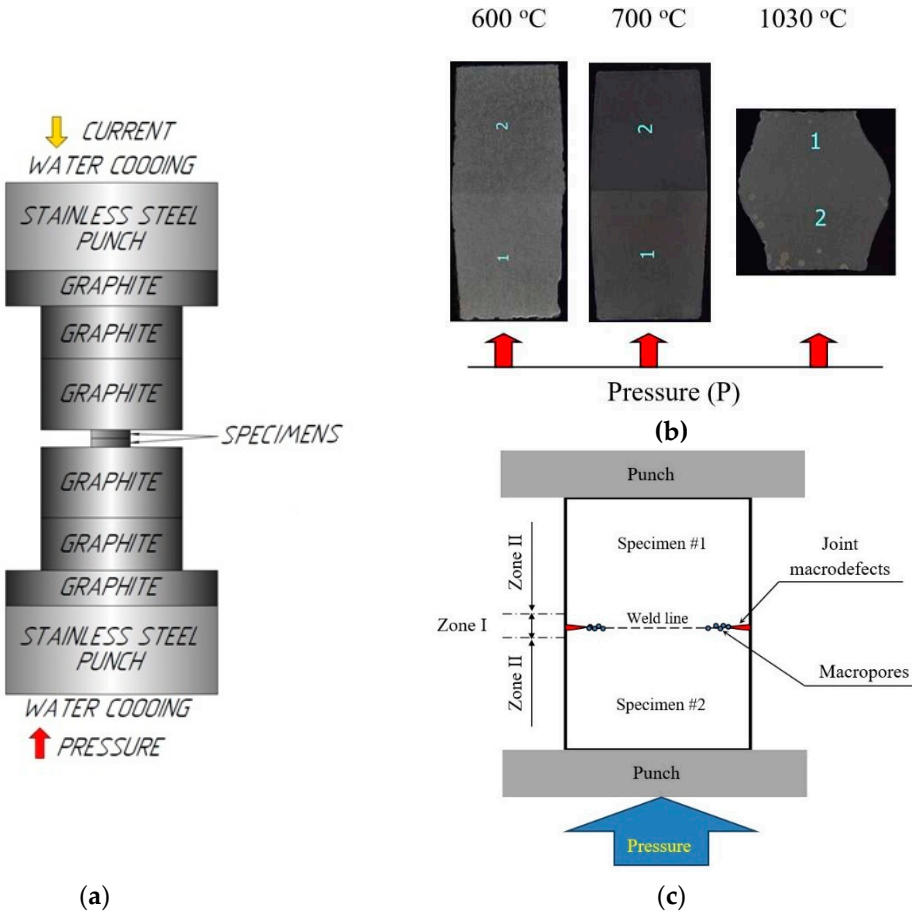

Figure 1. Scheme of diffusion welding of the titanium alloy specimens by SPS (**a**). Photographs of a coarse-grained specimens obtained at different diffusion welding temperatures (V_h = 100 °C/min, P = 50 MPa, t = 10 min) (**b**) and the locations of different zones in the cross-sections of the investigated specimens (**c**).

The microstructure studies were carried out using Jeol® JSM-6490 scanning electron microscope (SEM) with Oxford Instruments® INCA 350 energy dispersion spectroscopy (EDS) X-ray microanalyzer and Jeol® JEM-2100 transmission electron microscope (TEM) with JED-2300 EDS microanalyzer. The sizes of the elongated β-phase particles (d_β) and α-phase grains (d_α) was measured in two mutually perpendicular directions. The mean size was calculated by averaging the sizes in the longitudinal and transverse directions. Mean uncertainty of determining the sizes of the β-phase particles at the boundaries of the elongated α-grains was about 1 μm, in the region of the equiaxial α-grains – less than 0.5 μm. Mean uncertainty of determining the magnitude d_β in the present work was accepted to be 0.5 μm. The mean grain sizes d_α and d_β were determined by chord method using GoodGrains 2.0 software.

Preprints (www.preprints.org) | NOT PEER-REVIEWED | Posted: 27 January 2023 doi:10.20944/preprints202301.0501.v1

The microhardness *Hv* measurements were carried with Duramin® Struers™ 5 with the load of 2 kg. The microhardness measurements were performed along and across the welded joint line. The microhardness measured at the distance of 5 mm away from the weld line was accepted as the microhardness of the alloy. At this distance, the microhardness didn't change anymore, and the effect of the weld on the alloy microhardness should be minimized (see [51]).

Electrochemical studies were carried out in an aqueous solution of 10%HNO_3 + 0.2%HF with R-8 potentiostat-galvanostat (Electrochemical Instruments JSC, Russia). Testing was carried out in a glass electrochemical cell of 60 ml in volume, in a still solution. The temperature of testing was 30 °C. A chlorine-silver reference electrode (EVL-1M4) and a Pt wire as an auxiliary electrode were used in testing. Based on the analysis of the Tafel slope in the potentiodynamic curves [the potential E vs the current density i in the semilogarithmic axes ln(i) –E], the corrosion current density i_{cor} and the corrosion potential E_{cor} were calculated. Prior to testing, the surfaces of the specimens were subjected to mechanical polishing down to 3-5 μm roughness grade. Prior to the electrochemical tests, the specimen surfaces were covered by corrosion-resistant coating except a ~0.6 mm^2 (0.3×0.2 mm) open area located in the center of the specimen cross-section, in the weld area (Figure 2).

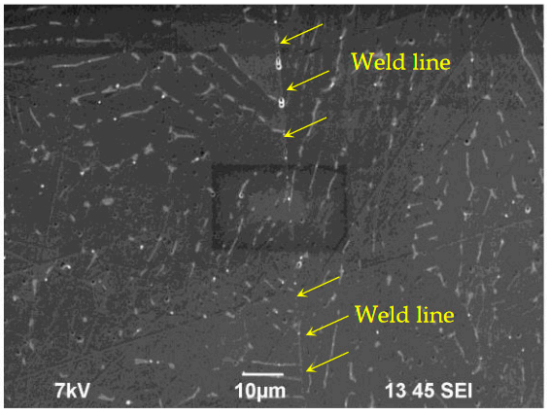

Figure 2. Position of the corrosion area relative to the welded joint. Specimen of the coarse-grained alloy (V_h = 10 °C/min, T = 700 °C, t = 10 min, P = 50 MPa) after the electrochemical testing. The joint line is marked by the yellow arrows. The corrosion area of 0.3×0.2 mm in size has darker borders. SEM.

Before starting the electrochemical tests, the specimens were kept in the electrochemical cell in the aqueous solution of 0.2%HF+10%HNO_3 until a stable open circuit potential was reached (the holding time was not less than 2 h). After wards, the $i(E)$ curve was measured at the potential scanning rate of 0.5 mV/s. Scanning was performed in the potential range from –800 mV to –350 mV. Mean uncertainty of determining E_{corr} was 5 mV and was limited by the reproducibility of the results. The uncertainty of determining the corrosion current density i_{corr} varied since it depended on the uncertainty of determining the corrosion area, on the uncertainty of determining the slope by least mean squares method, and on the reproducibility of the results. Mean uncertainty of determining i_{corr} was close to 0.1-0.15 mA/cm^2. The reproducibility of the results was determined by measuring the $i(E)$ curves three times for each specimen as well as by comparing the results for several specimens welded in the same regime (V_h = 100 °C/min, T = 700 °C, t = 10 min, P = 50 MPa).

The HSC tests were performed in a mixture of the crystal salts NaCl and KBr mixed in the proportion 300:1. The testing was performed at the temperature 250 °C in the conditions of access of oxygen. The accuracy of the temperature stabilization was ±5°C. The testing was performed in laboratory autoclaves with the internal volume 3000 cm^3 providing an opportunity of the access of the ambient air (see [65]). Prior to the testing, the surfaces of the specimens underwent the mechanical polishing down to the roughness level of 3-5 μm. To perform the testing, the specimens were placed in the centers of ceramic bowls with the internal volume of 600 cm^3 providing the access of ambient air. The mixture of crystal salts prepared in advance in necessary proportion was put inside the bowls. The ceramic bowls with the specimens inside the mixed salts were placed in the centers of the testing autoclaves. The HSC testing time was 500 h. The character of the corrosion defects of the

Preprints (www.preprints.org) | NOT PEER-REVIEWED | Posted: 27 January 2023 doi:10.20944/preprints202301.0501.v1

specimen surfaces was evaluated with Leica® DM IRM optical microscope. The classification of the emerging corrosion defect type was performed according to the requirements of Russian National Standard GOST 9.908-85. In order to describe the degree of corrosion damage of the titanium alloy surfaces, we used the criteria of the average depth of the corrosion defects (h_{av}) and of the maximum one (h_{max}). The mean depths of the corrosion defects were determined by averaging of the depths of not less than 10 defects.

X-ray diffraction (XRD) investigations were carried out using Shimadzu® XRD-7000 diffractometer. The investigation technique was described in [66]. The measurement regime was as follows: exposure time Δt = 0.6 s, angular step $\Delta 2\theta$ = 0.04°, no slit before the detector. The salt contamination surfaces were nonuniform that affected the quality of the XRD signal negatively. Therefore, the investigations of the phase composition of the resulting products of the hot salt corrosion of the titanium alloys were performed in two regimes: (i) direct analysis of the composition of the salt contamination lifted off the specimen surface mechanically itself and (ii) the analysis of the composition of the corrosion products formed on the specimen surface. For the investigations in the regime (ii), the corrosion products were washed out from the specimen surfaces in a flow of a hot water during 10 min. After rinsing, the dark-colored non-solvable corrosion products remained on the specimen surfaces.

3. Results

3.1. Microstructure and properties of the alloy in the initial state

The results of investigations of the microstructure of the UFG alloy Ti-5Al-2V were described in details in [26]. Here we list briefly main results, which will be necessary for further analysis.

In the initial state, the microstructure of the Ti-5Al-2V alloy comprises typical mixture of grains of α-phases (Figure 3a). The mean sizes of the elongated α-phase grains are 10-20 μm (Figure 3b), the mean size of the equiaxial α-phase grains are 50-100 μm (Figure 3a, see [26]). At the grain boundaries (GBs) of the elongated α-phase, there are the elongated β-phase grains are ~10-15 μm long and less than 1 μm in thickness (Figure 3b). The volume fraction of the β-phase particles was small enough and was not detected by XRD phase analysis.

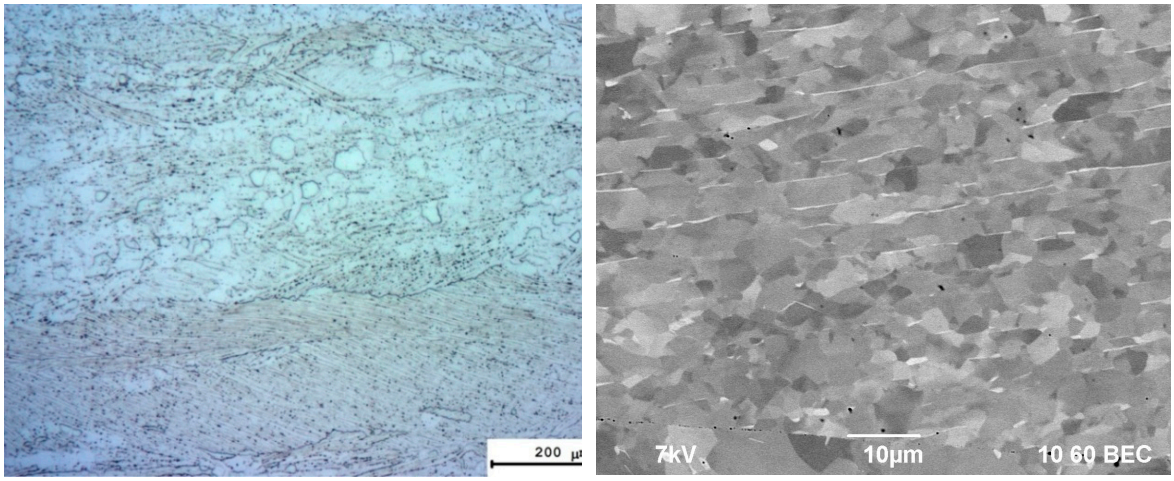

(a) **(b)**

Preprints (www.preprints.org) | NOT PEER-REVIEWED | Posted: 27 January 2023 doi:10.20944/preprints202301.0501.v1

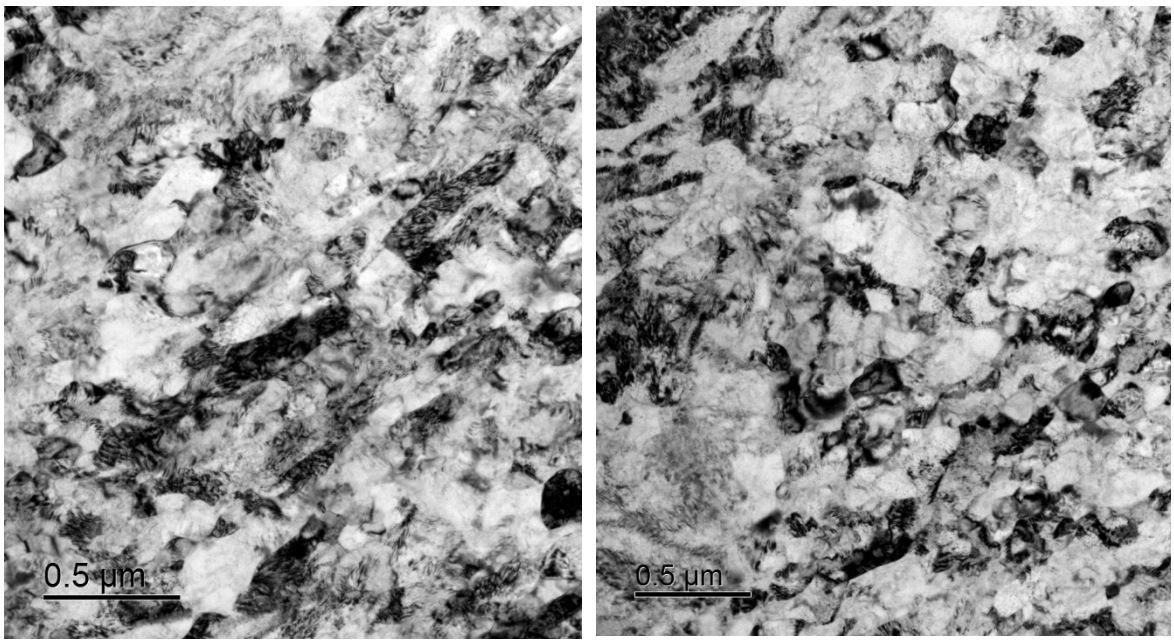

(c) **(d)**

Figure 3. Microstructure in the coarse-grained (**a, b**) and UFG (**c, d**) alloy Ti-5Al-2V [26,50].

Two types of GBs were observed in the coarse-grained alloy Ti-5Al-2V. The GBs of the first type are the pure ones (~90-95 vol.%), in which the grain boundary segregation of aluminum or vanadium is absent (Figure 4a, [26]). The averaged local aluminum concentration at such GBs was 3.8 ± 0.9 wt.% and the concentration of vanadium was 1.9±0.2 wt.% that differed from the concentrations of these elements in the crystal lattice insufficiently: the local concentration of aluminum in the GBs was 3.6±0.9 wt.% and the local concentration of vanadium was ~1.4 ± 0.2 wt.%. The GBs of the second type are the ones with the vanadium segregations, in which the local concentration of vanadium may achieve 10 wt.% (Figure 4b, [26]). Mean concentration of aluminum in the crystal lattice near the GBs of the II type was ~4 wt.%, the concentration of vanadium was ~1.6 wt.%.Note also that in the β-phase particles local concentration of vanadium achieved 16-18%, the concentration of aluminum was less than 1 wt.% (Figure 4c, [26]).

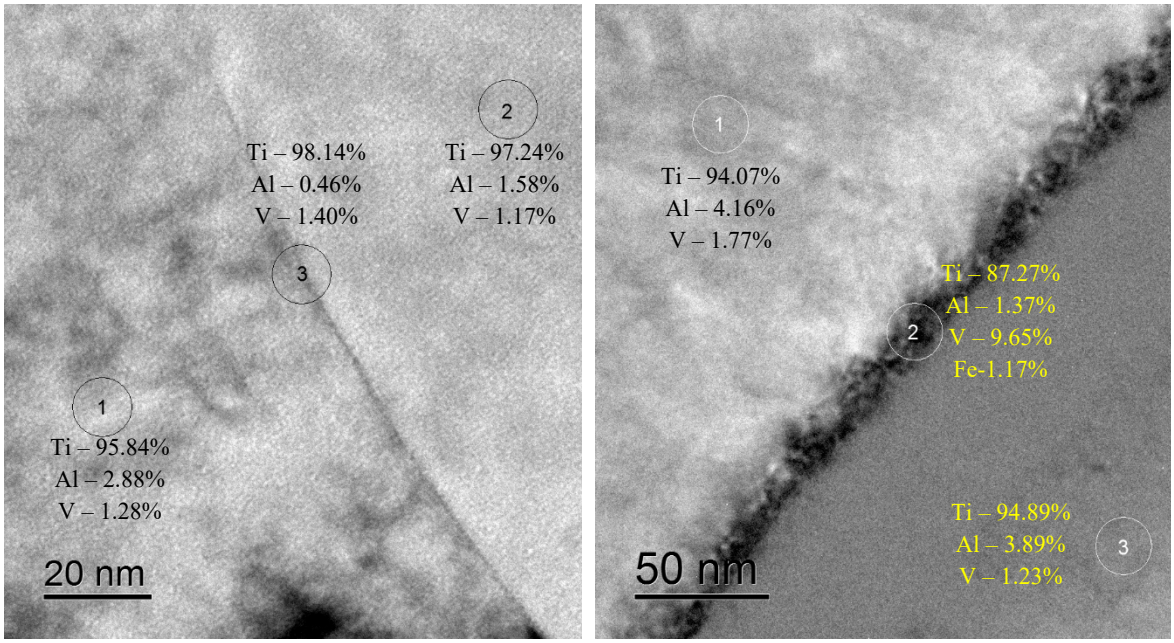

(a) **(b)**

Preprints (www.preprints.org) | NOT PEER-REVIEWED | Posted: 27 January 2023 doi:10.20944/preprints202301.0501.v1

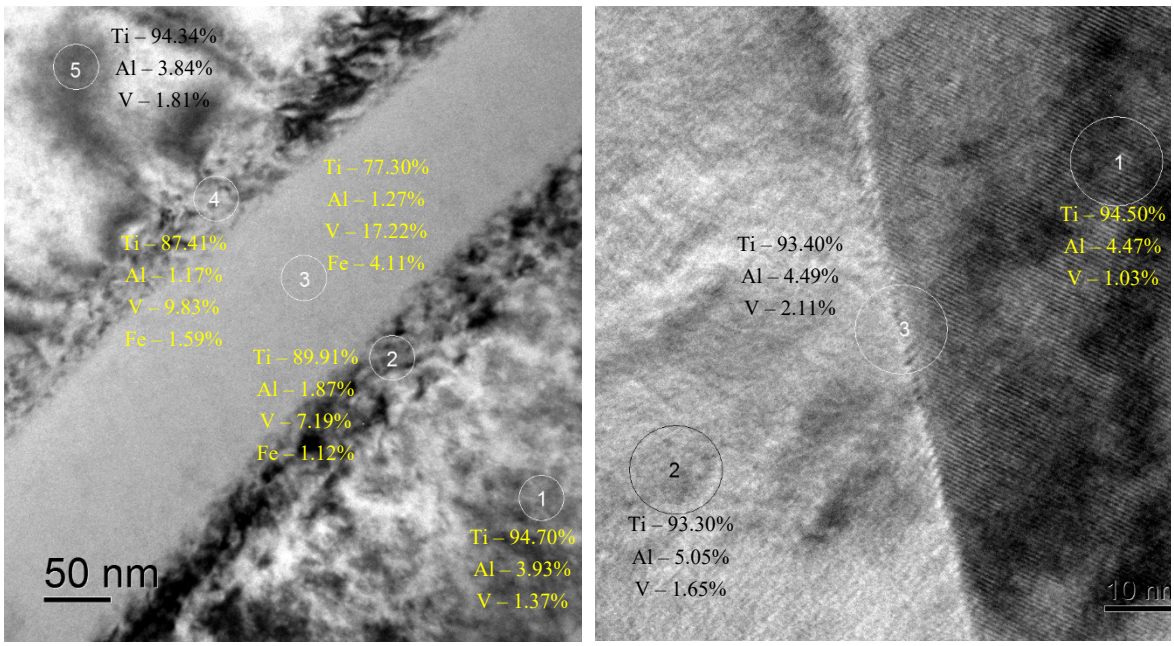

(c) **(d)**

Figure 4. EDS microanalysis of the grain boundary composition in the coarse-grained (**a, b, c**) and UFG (**d**) alloy Ti-5Al-2V [26,50]. TEM.

In the course of ECAP, a uniform grain microstructure with mean grain size 0.3-0.5 μm was formed (Figure 3c,d). The grains had an equiaxial shape. The grain boundary segregations of vanadium analogous to the ones observed in the coarse-grained alloy were not observed (Figure 4d, [26]). Mean concentration of aluminum at the GBs in the UFG alloy was ~3.2 ± 0.8 wt.%, in the crystal lattice it was ~4.0 ± 0.8 wt.%. Mean concentration of vanadium at the GBs in the UFG alloy was ~1.9 ± 0.3 wt.%, in the crystal lattice it was ~1.5 ± 0.3 wt.%. The β-phase large particles at the GBs in the UFG alloy after ECAP were not observed. As it has been shown in [26], the decreasing of the local concentration of vanadium at the GBs as well as the absence of the β-phase particles are the origins of increased resistance of the UFG alloy Ti-5Al-2V to the intercrystalline hot salt corrosion (Tables 2 and 3).

3.2. Macrostructure of the specimens after diffusion welding

The investigations of the macrostructure of the specimens have shown the presence of the incompletely welded joint areas (macrodefects) of ~50-70 μm in size at the edges of the coarse-grained specimens obtained by SPS at low stress, low temperatures, or increased heating rates (Figure 5d, 6a;see Zone I in Figure 1c). Such macrodefects may promote a crevice corrosion, therefore, the presence of these ones is undesirable. As a rule, large enough pores were located at the apices of the joint macrodefects. The volume fraction of the pores dropped with increasing distance from the specimen edges (i. e. from the maximum tensile strain area) abruptly. The length of the area with macropores depended on the welding regimes and ranged from 10μm up to 100 μm (Figure 6c, e). In the rest (larger) area of the welded joints, there were micropores of the submicron sizes. The volume fraction of these ones depended on the diffusion welding regimes. Also, there were some individual macropores of ~1-2 μm in size (Figure 6e). Note that a small volume fraction of the macro- and micropores was observed in the case of the diffusion welding of the coarse-grained specimens in the interval of moderate temperatures (700-800 °C) and at low stresses (50 MPa), when the plastic deformation doesn't lead to the strain-induced pore formation yet.

Preprints (www.preprints.org) | NOT PEER-REVIEWED | Posted: 27 January 2023 doi:10.20944/preprints202301.0501.v1

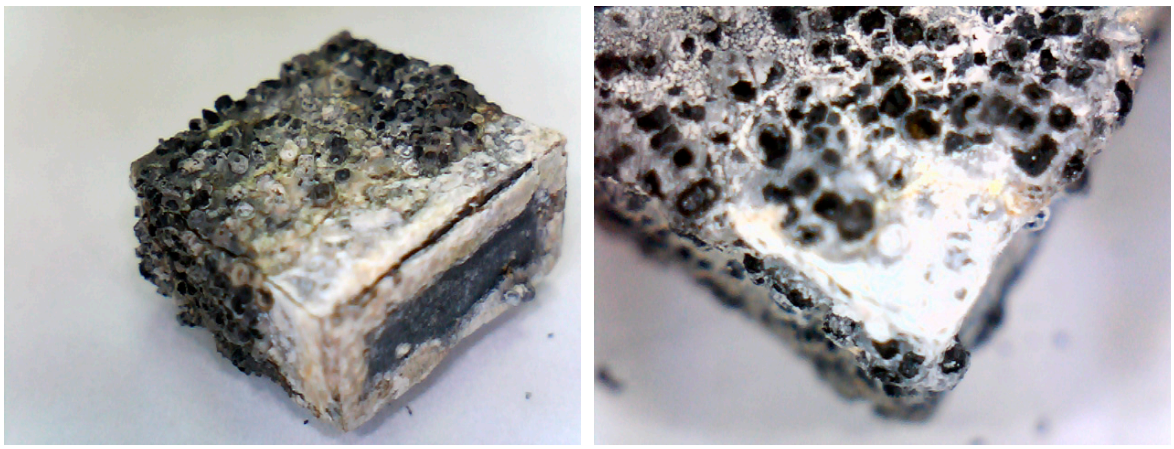

(a) (b)

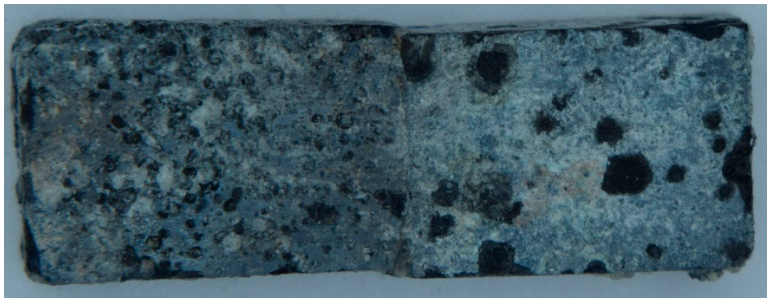

(c)

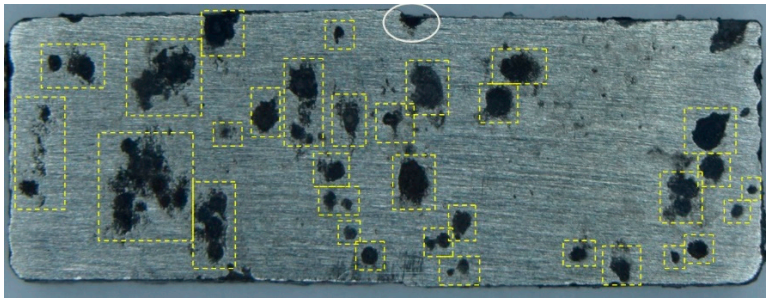

(d)

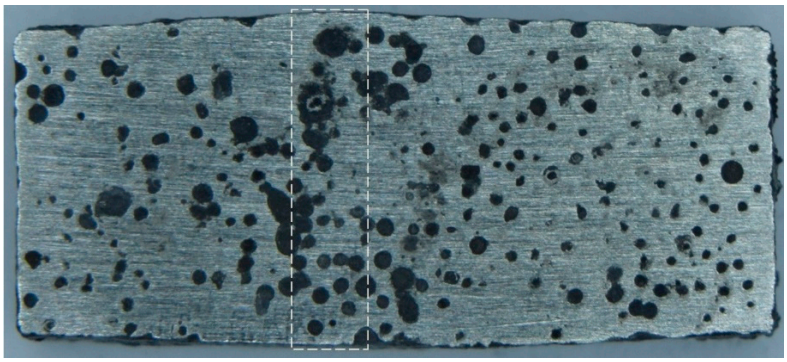

(e)

Figure 5. Photographs of the alloy specimens after hot salt corrosion testing (**a, b**), after rinsing in a hot water flow (**c**), and after mechanical polishing (**d, e**). In Figure 5**d**, the largest corrosion pits are highlighted by yellow dashed line, the white solid line outline a joint macrodefect, which the crevice corrosion and the pitting one go through simultaneously. In Figure 5**e**, the welded joint area (Zone I, see Figure 1**c**) is outlined by white dashed line.

Preprints (www.preprints.org) | NOT PEER-REVIEWED | Posted: 27 January 2023 doi:10.20944/preprints202301.0501.v1

In the specimens of the UFG titanium alloys welded with SPS, the macrodefects of joints were much smaller in sizes (Figure 6b). The volume fractions of the macro- and micropores were in the welds of the UFG specimens were smaller than in the welds of the coarse-grained ones (Figure 6d,f; Figure 7); the large pores ones were observed preferentially in the case of the diffusion welding at low temperatures (600 °C) or at high stresses (70-100 MPa). In most cases, a highly dense microstructure is formed when welding the specimens of UFG Ti alloys, which the sizes and the volume fraction of the pores in Zone II (Figure 1c) are small (Figure 7). In the optimal welding regimes of the UFG specimens, the weld lines are hardly visible (Figure 7). It was caused by differences in the mechanisms of high temperature deformation in SPS of the coarse-grained and UFG alloys as well as by the effect of accelerated diffusion delocalization of pores in the high-speed heating modes (for more details, see [50]).

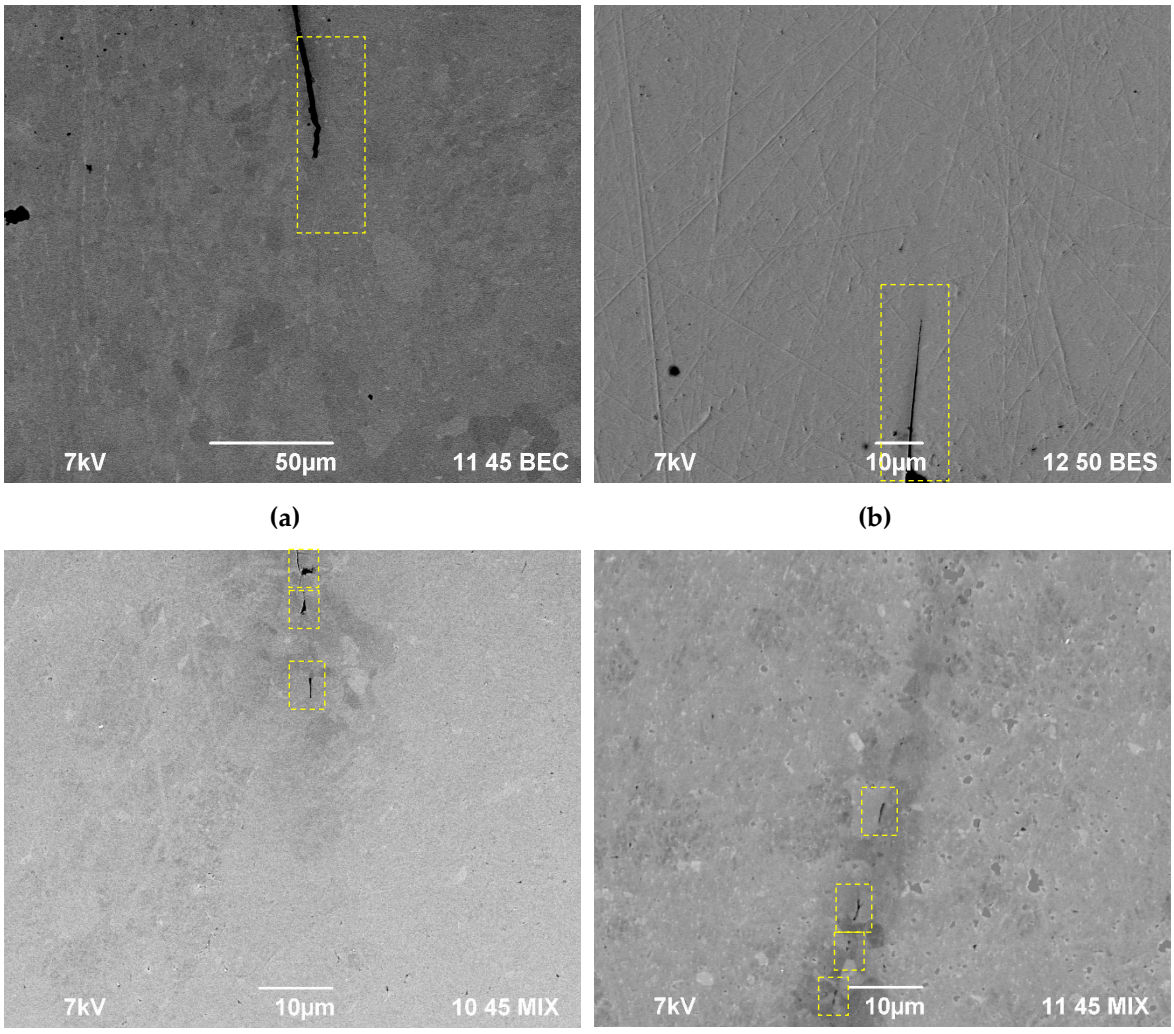

(a) **(b)**

(c) **(d)**

Preprints (www.preprints.org) | NOT PEER-REVIEWED | Posted: 27 January 2023 doi:10.20944/preprints202301.0501.v1

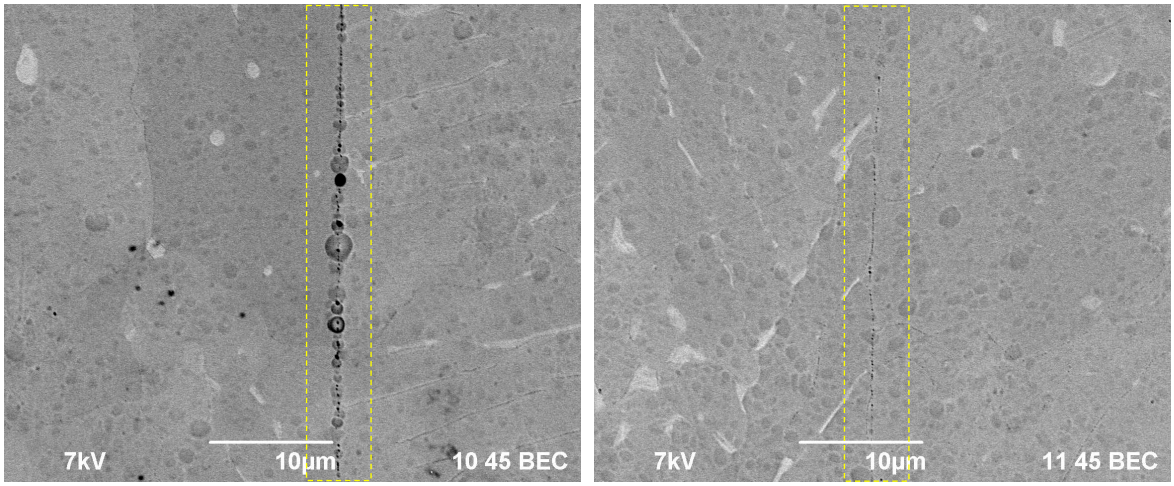

(e) **(f)**

Figure 6. Typical defects in the welded joints of the coarse-grained (**a, c, e**) and UFG (**b, d, f**) alloy after the diffusion welding (V_h = 50 °C/min, T = 800 °C, t = 10 min): (**a, b**) a joint defect, (**c, d**) a macropore, (**e, f**) a micropore. SEM.

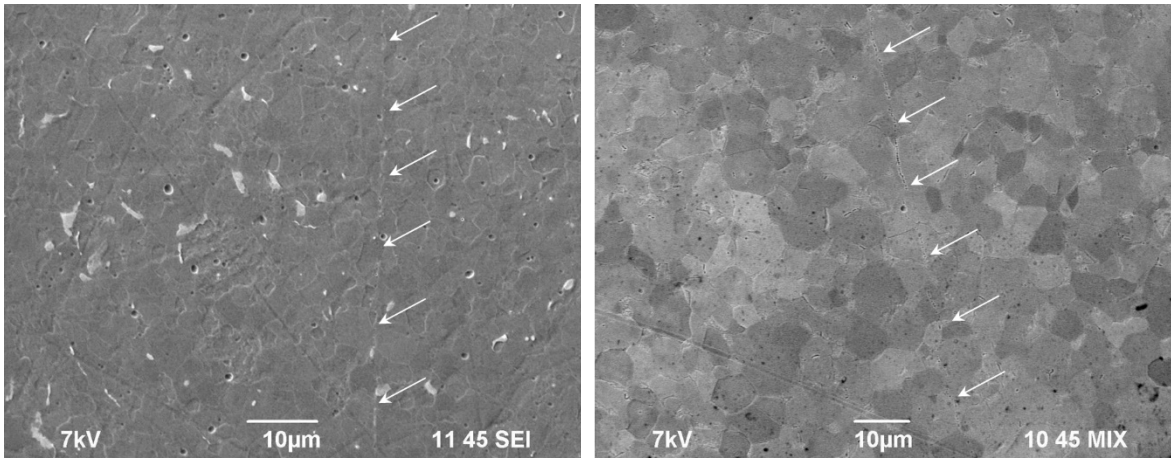

(a) **(b)**

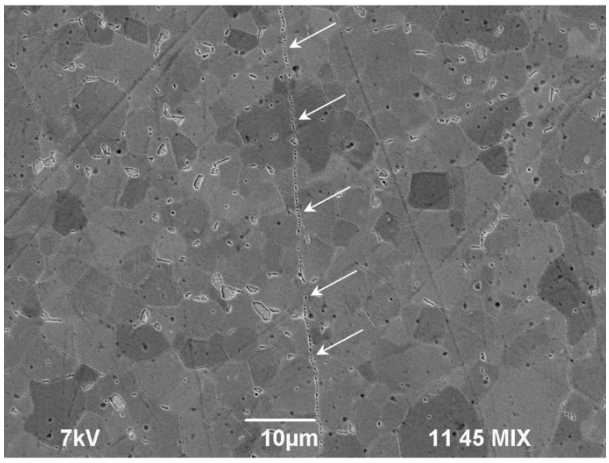

(c)

Figure 7. Micropores in the welded joints of the UFG titanium alloy after diffusion welding (t = 10 min, P = 50 MPa): (**a**) V_h = 50 °C/min, T = 600 °C; (**b**) V_h = 350 °C/min, T = 700 °C; (**c**) V_h = 50 °C/min, T = 800 °C. SEM.

Preprints (www.preprints.org) | NOT PEER-REVIEWED | Posted: 27 January 2023 doi:10.20944/preprints202301.0501.v1

3.3. Microstructure of specimens after diffusion welding

The results of investigations of the microstructure of the welded joints in the specimens of the coarse-grained titanium alloy Ti-5Al-2V have shown the varying of the main parameters of the diffusion welding (the heating rate from 10 up to 350 °C/min, the welding temperature from 600 up to 800 °C, the holding time from 0 up to 90 min, the magnitude of applied stress from 30 up to 100 MPa) does not affect the mean grain size considerably (Table 2). The only exception was welding at the temperatures 1040 and 1140 °C exceeding the temperature of $\alpha \leftrightarrow \beta$ phase transition: the microstructure of the specimens obtained by diffusion welding at increased temperatures was featured by a martensite-type needle-like microstructure (see Figure 17 in [50]).

Table 2. Parameters of microstructure and microhardness of the PT-3V alloy specimens after the diffusion welding.

No.	Welding regime				Coarse-grained alloy					UFG alloy				
	T, °C	V_h, °C/min	t, min	P, MPa	d_α, μm	d_β, μm	Weld porosity (Zone II)	*Hv*, GPa Weld	*Hv*, GPa Alloy	d_α, μm	d_β, μm	Weld porosity (Zone II)	*Hv*, GPa Weld	*Hv*, GPa Alloy
0	State before welding				10-100	3-15	-	-	2.0-2.1	0.5	-	-	-	3.1-3.2
1	600				~16	3.2	High	2.5	2.4-2.5	4.8	2.4	High	3.0	3.0-3.1
2	700				~17	3.0	Medium	2.5	2.5-2.6	5.9	3.0	Low	2.8	2.8-2.9
3	800	100	10	50	~18-19	5.1	Medium	2.3	2.3-2.4	6.9	3.3	Medium	3.2	3.2
4	1030				~12	-	Low	2.5	2.4	-	-	-		
	1142				-	-	-	-	-	5.2		Low	2.6	2.6-2.7
5		10			~16-18	5.0	Low	2.6	2.5	6.8	3.1	High	2.5	2.5-2.6
6	700	50	10	50	~17-18	3.5	Medium	2.6	2.4-2.3	5.5	3.3	Medium	2.7	2.8-2.9
7		100			~18-19	3.0	Medium	2.4	2.5	5.9	3.0	Low	2.7	2.7-2.9
8		350			~18	3.0	High	2.4	2.5	3.8	3.3	Low	2.9	3.0-3.1
9				50	~18-19	3.5	Medium	2.5	2.4-2.6	5.9	3.3	Low	2.7	2.8-2.9
10	700	100	10	70	~15	3.2	High	2.7	2.6-2.7	5.3	2.6	High	2.7	2.9-3.0
11				100	~10	2.9	High	2.7	2.5-2.6	4.9	2.5	High	2.7	3.0-3.1
12			0		~18-19	3.5	High	2.5	2.5-2.6	4.7	2.0	High	2.9	2.9-3.1
13	700	100	10	50	~18-19	3.0	Medium	2.4	2.4-2.5	5.9	3.3	Medium	2.7	2.8-2.9
14			50		~16-17	2.0	Medium	2.3	2.3-2.6	9.1	3.5	Low	2.6	2.8
15			90		~12-13	2.0	Medium	2.4	2.4-2.6	9.3	3.5	Low	2.5	2.5-2.6

The alloy microstructure near the welded joint was featured by a coarse-grained mixed α-structure, the nucleation of the β-particles was observed at the GBs (Figure 8). The most intensive nucleation of the β-phase particles was observed at the boundaries of the elongated α-phase grains, the volume fraction of the β-phase particles at the boundaries of the equiaxial α-phase grains was low (Figure 8c,d). In the case of welding at reduced temperatures, the sizes and volume fraction of the β-phase particles in the coarse-grained welded joint material appeared to be close to the parameters of the β-phase particles in the initial state (Figure 8a,c,d; Figure 3b). Fast heating up to the temperatures corresponding to the two-phase (α+β) region (800 °C) and to β-region (1030 °C) followed by cooling down to room temperature resulted in the increasing of the sizes and of the volume fraction of the β-phase particles (Figure 8b). The increasing of the heating rate, of the applied stress magnitude, and of the isothermic holding time results in the decreasing of the mean size of the β-phase elongated particles (Table 2, Figure 8b).

Preprints (www.preprints.org) | NOT PEER-REVIEWED | Posted: 27 January 2023 doi:10.20944/preprints202301.0501.v1

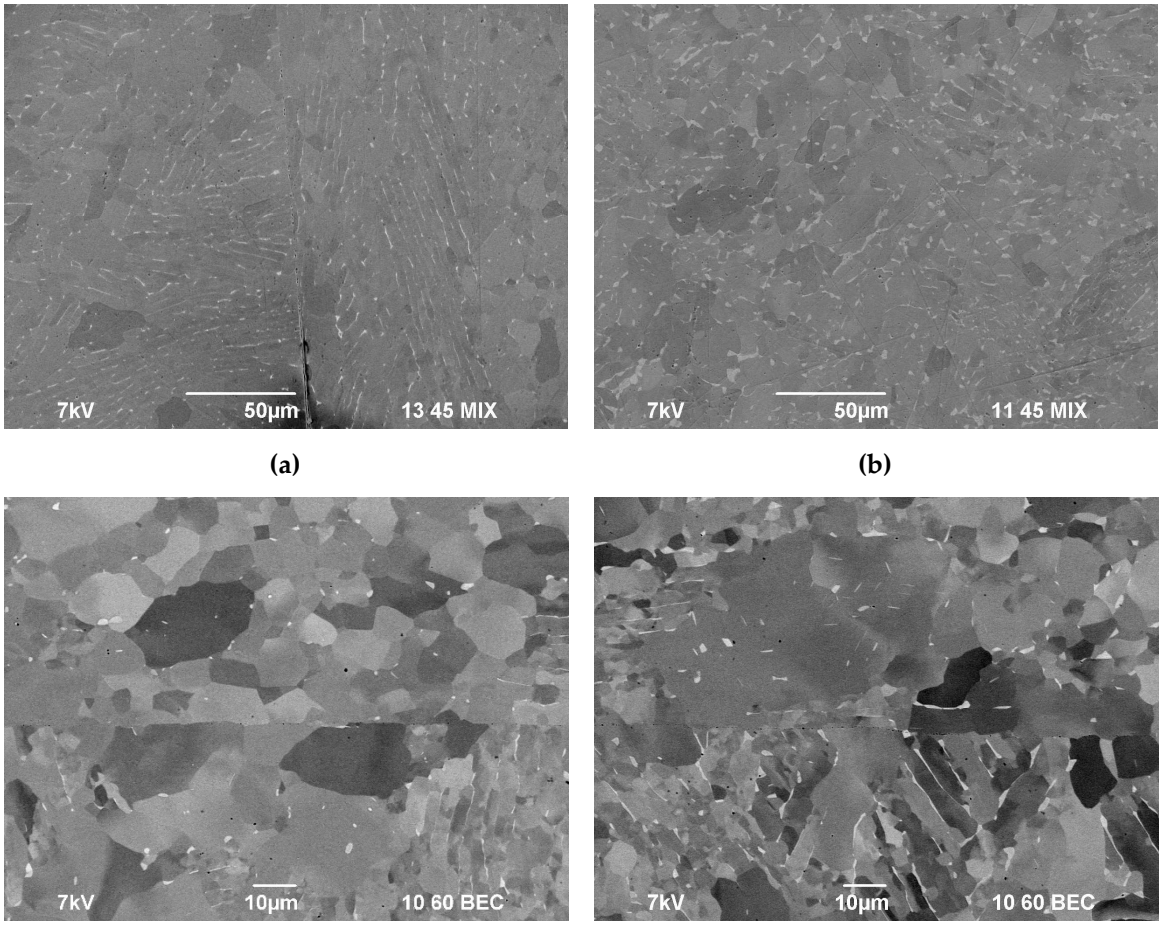

Figure 8. Microstructure of the specimens of the coarse-grained alloy in the initial state and the microstructure of the specimens obtained in different regimes of the diffusion welding (P = 50 MPa, t = 10 min): (**a**) V_h = 50 °C/min, T = 600 °C; (**b**) V_h = 50 °C/min, T = 800 °C; (**c**) V_h = 100 °C/min, T = 700 °C; (**d**) V_h = 350 °C/min, T = 700 °C. SEM.

The parameters of microstructure of the UFG welded specimens are presented in Figure 9 and in Table 2. The metallographic and SEM investigations of the welded joints in the specimens of the UFG alloys demonstrated the increasing of the welding temperature from 600 °C up to 800 °C (at V_h = 50 °C/min, P = 50 MPa, t = 10 min) to result in the increasing of the mean grain size d_α from 4.8 μm up to 6.9 μm (see Figure 17 in [50]). Also, it is worth noting that the mean grain size d_α in the welded joints of the UFG specimens appeared to be 1.5-3 times less than the main grain size in the welded joints of the coarse-grained specimens (Figure 9). There were some individual β-phase particles at the GBs, the sizes of which were 2-3 μm (Figure 9a,b,d,e). Note that the increasing of the welding temperature and of the isothermic holding time (at T = 700 °C) results in the increasing of the β-phase particle size d_β and of the sizes the titanium alloy grains d_α (Table 2). The increasing of the heating rate from 10 up to 350 °C/min didn't affect the β-phase grain sizes considerably but resulted in the decreasing of the mean titanium alloy grain sizes (Table 2).

Preprints (www.preprints.org) | NOT PEER-REVIEWED | Posted: 27 January 2023 doi:10.20944/preprints202301.0501.v1

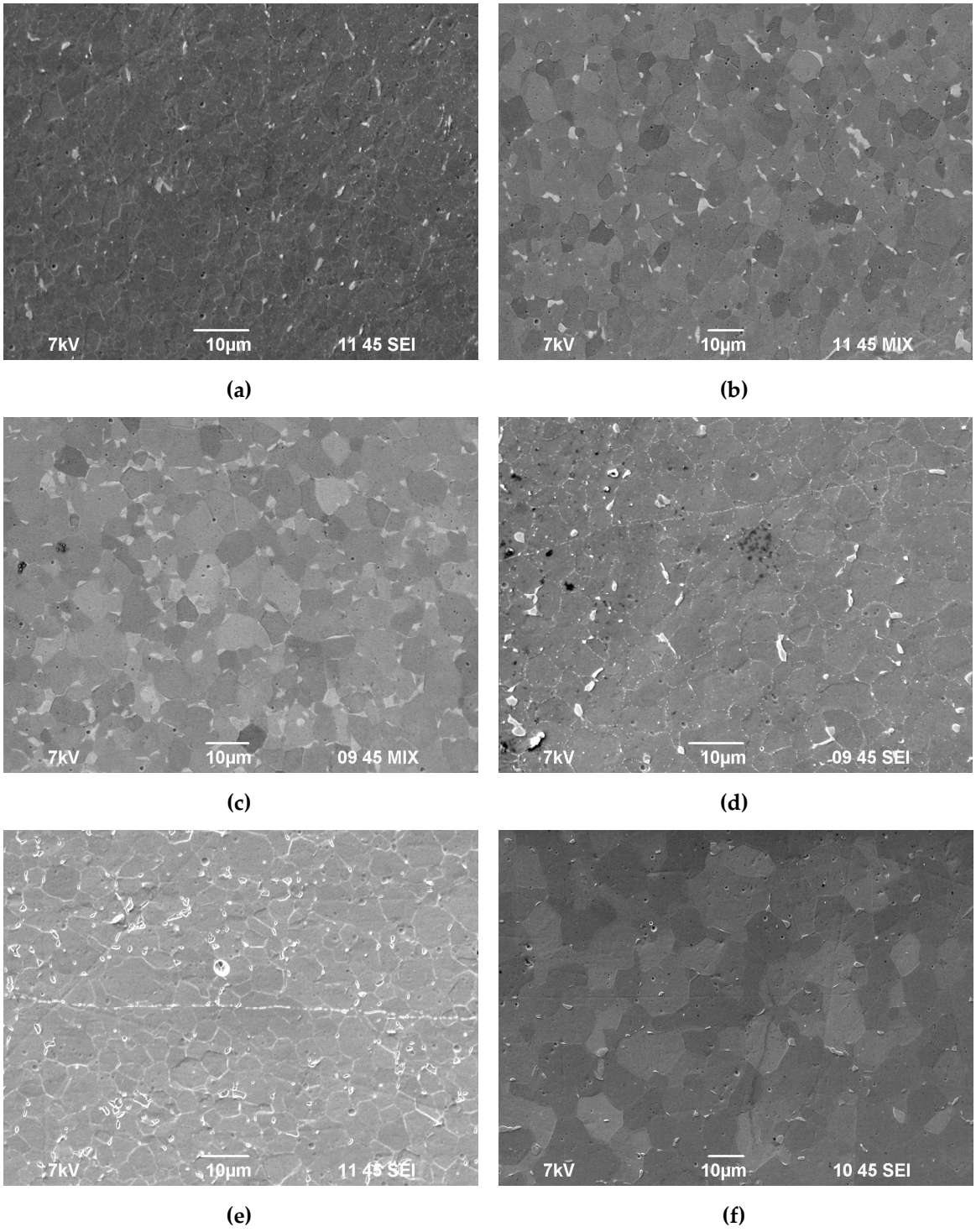

Figure 9. Microstructure of the specimens of the UFG alloy obtained in different diffusion welding regimes (P = 50 MPa): (**a**) V_h = 50 °C/min, T = 600 °C, t = 10 min; (**b**) V_h = 50 °C/min, T = 700 °C, t = 10 min; (**c**) V_h = 50 °C/min, T = 800 °C, t = 10 min; (**d**) V_h = 100 °C/min, T = 700 °C, t = 10 min; (**e**) V_h = 350 °C/min, T = 700 °C, t = 10 min; (**f**) V_h = 50 °C/min, T = 700 °C, t = 90 min. SEM.

3.4. Hot salt corrosion test

Photographs of the specimens after the HSC testing are presented in Figure 5. A porous character of the salt contamination (Figure 5a,b) evidences the formation of gaseous $TiCl_4$ in the course of the HSC (see [54]). The XRD phase analysis demonstrated the presence of rutile phase TiO_2, $Na_4Ti_5O_{12}$, and NaCl on the surface of the coarse-grained and UFG specimens alloys Ti-5Al-2V (Figure 10).

Preprints (www.preprints.org) | NOT PEER-REVIEWED | Posted: 27 January 2023 doi:10.20944/preprints202301.0501.v1

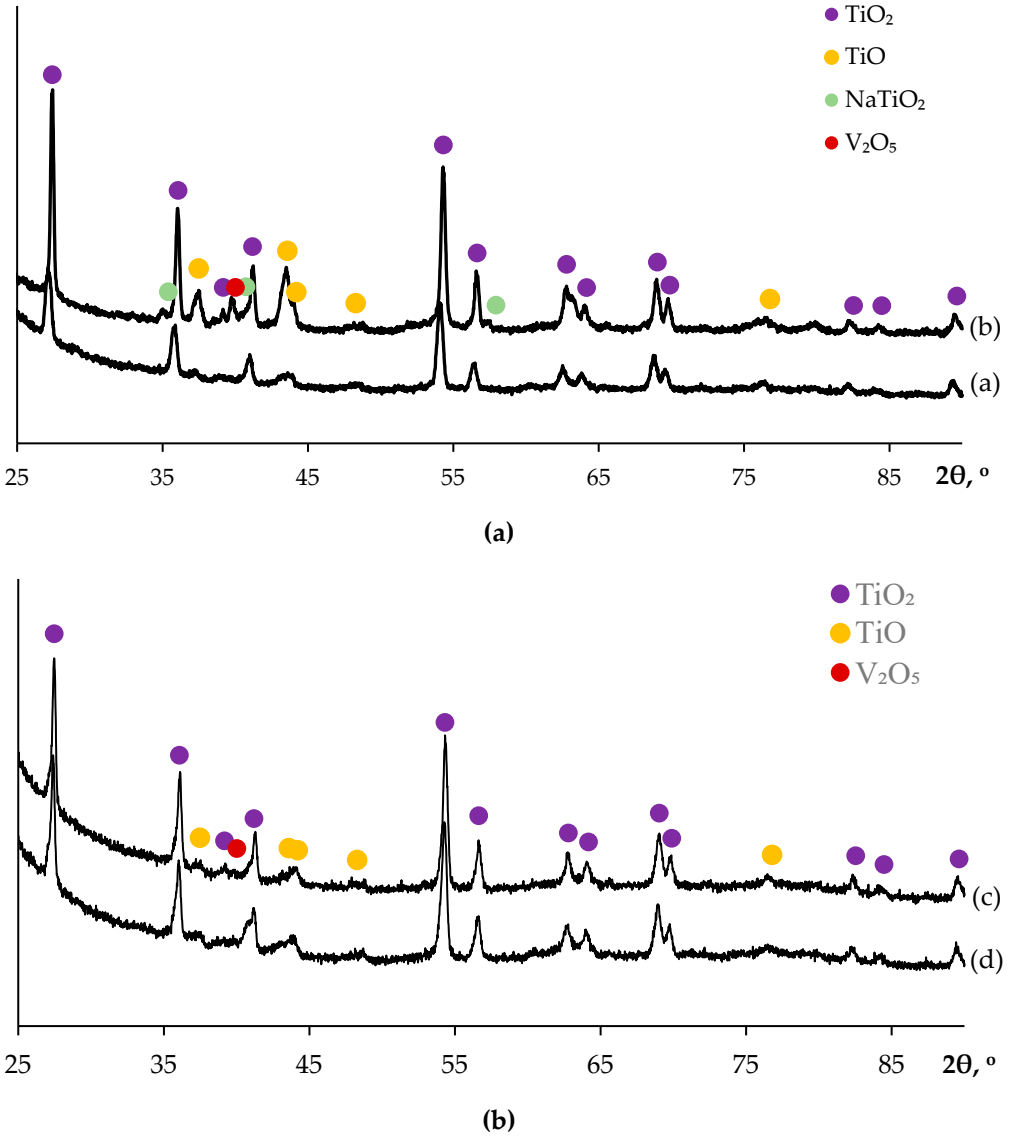

Figure 10. Results of XRD analysis of the corrosion products on the surfaces of the specimens of coarse-grained (a) and UFG (b) alloys after HSC testing.

In most cases, the salt contaminations on the specimen surfaces are the mixtures of NaCl (ICDD 00-005-0628), titanium oxides TiO_2 (ICDD 00-015-0875) and TiO (ICDD 01-072-0020), and alumina (ICDD 01-075-0278) as well as of the vanadium-based phases - $VO_{1.15}$ (ICDD 01-073-9519), $V_2Ti_3O_9$ (ICDD 00-030-1429), and Al_3V (ICDD 01-079-5717) (see Figure 11). The products of corrosion (salt contaminations) on the samples obtained by the diffusion welding at the temperatures greater than 1000 °C also consisted of NaCl, TiO_2, TiO, and alumina but instead of the vanadium-based phases ($VO_{1.15}$, $V_2Ti_3O_9$, Al_3V), the aluminum-containing phases ($TiAl_2Cl_8$ phase (ICDD 01-076-1072) and intermetallic compound $AlTi_3$ (ICDD 00-052-0859) as well as traces of vanadium oxide VO_2 (ICDD 03-065-7960) were observed (Figure 11).

The results of investigation of the macrostructure of the welded joint cross-sections demonstrated the mechanisms of corrosion destruction of the metal in the welded joint areas and far away of these ones to be different (Table 3, Figure 12).

Preprints (www.preprints.org) | NOT PEER-REVIEWED | Posted: 27 January 2023 doi:10.20944/preprints202301.0501.v1

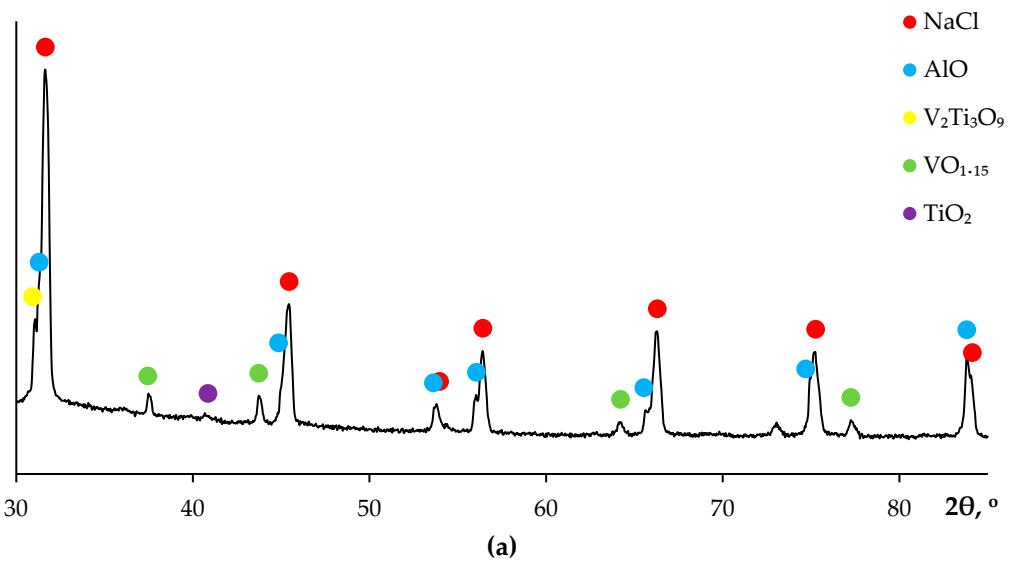

(a)

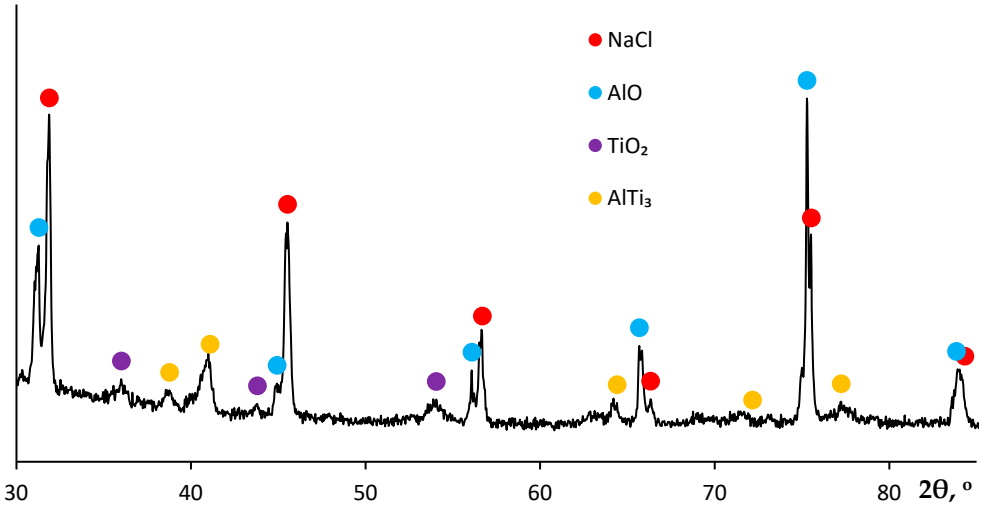

(b)

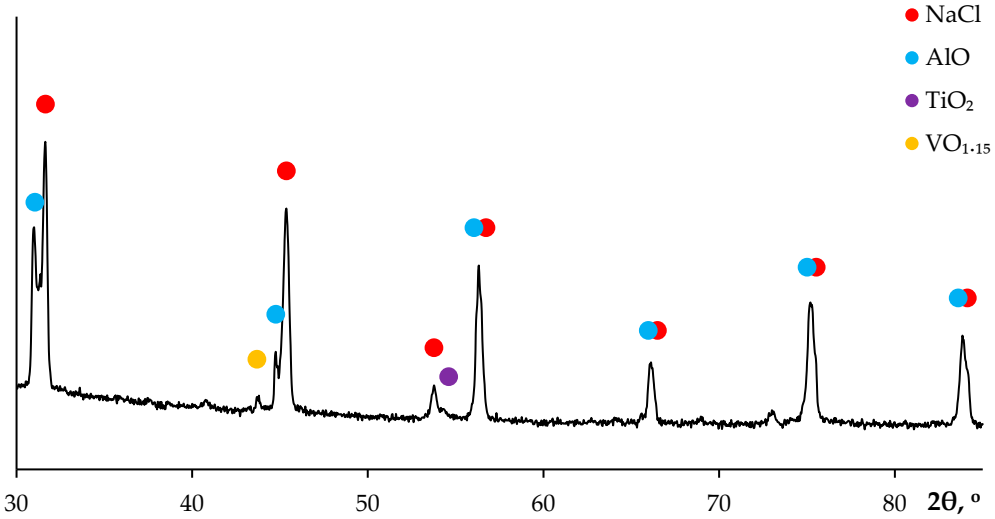

(c)

Preprints (www.preprints.org) | NOT PEER-REVIEWED | Posted: 27 January 2023 doi:10.20944/preprints202301.0501.v1

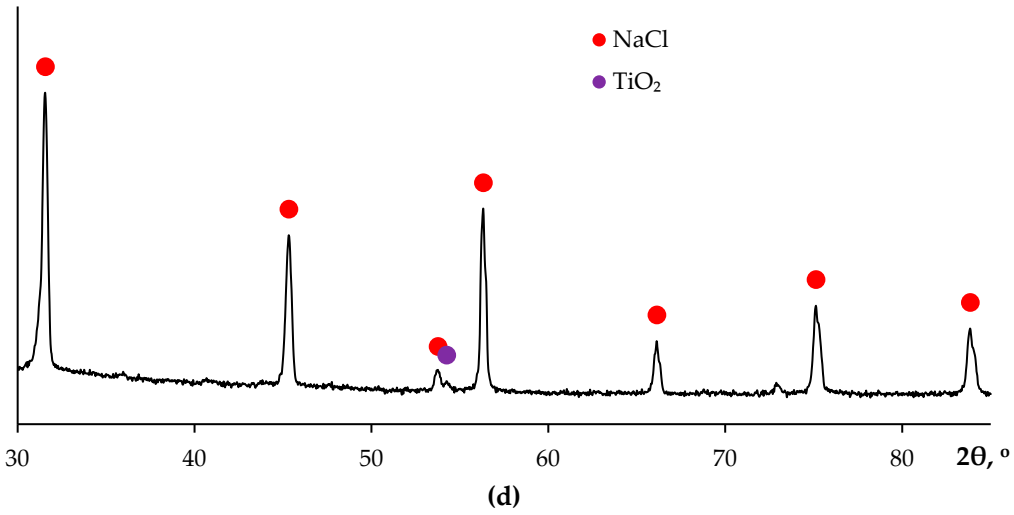

(d)

Figure 11. Results of XRD compositional and phase analysis of the salt contaminations on the surfaces of specimens of the coarse-grained (**a, b**) and UFG (**c, d**) alloys after HSC testing: (**a, c**) V_h = 50 °C/min, T = 600 °C, t = 10 min, P = 50 MPa; (**b**) V_h = 50 °C/min, T = 1030 °C, t = 10 min, P = 50 MPa; (**d**) V_h = 50 °C/min, T = 1140 °C, t = 10 min, P = 50 MPa.

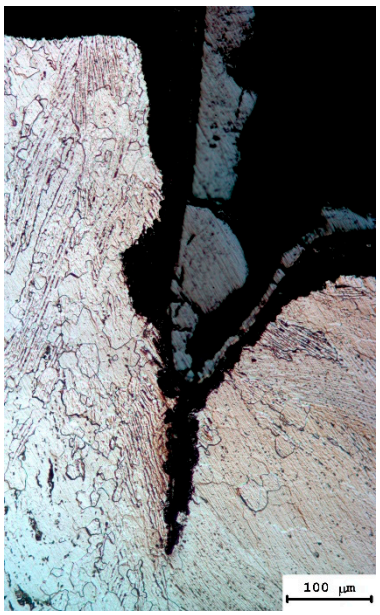

(a)

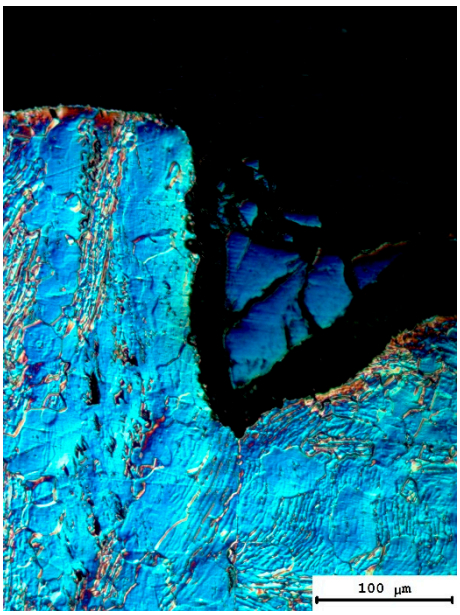

(b)

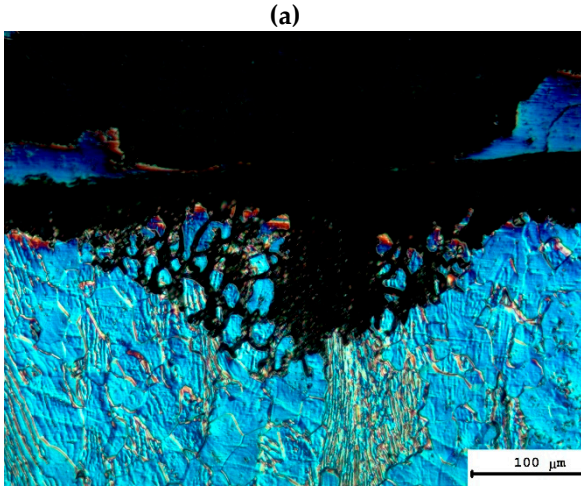

(c)

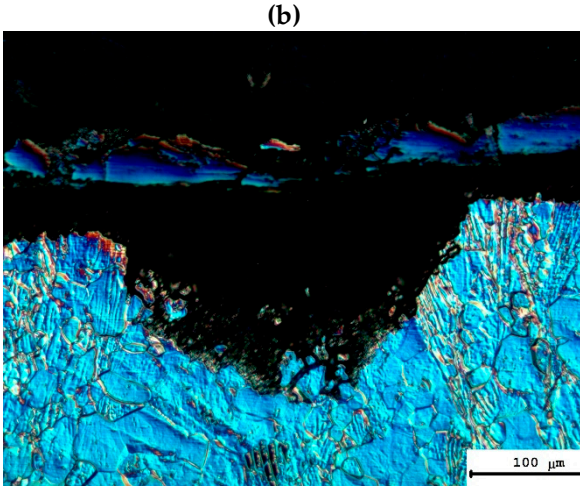

(d)

Preprints (www.preprints.org) | NOT PEER-REVIEWED | Posted: 27 January 2023 doi:10.20944/preprints202301.0501.v1

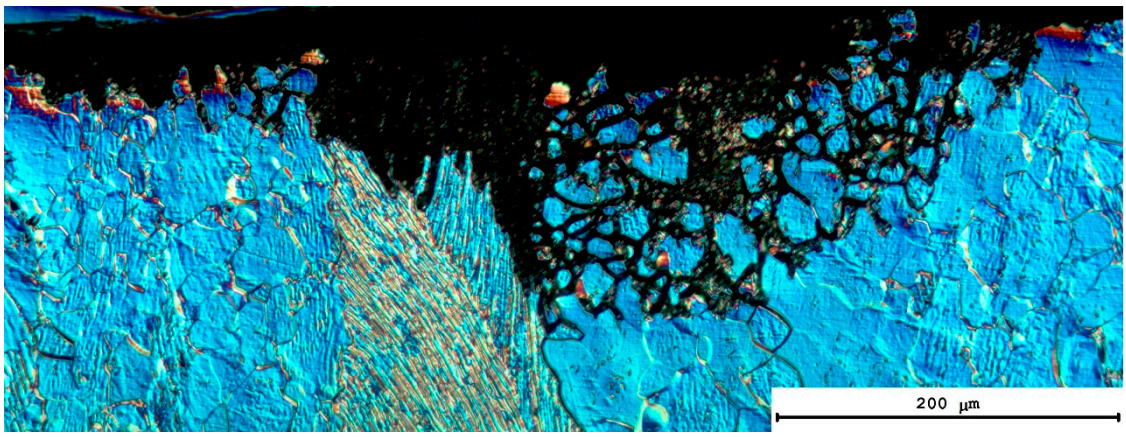

(e)

Figure 12. Corrosion defects on the surfaces of the coarse-grained titanium alloy specimens after HSC testing: (**a, b**) crevice corrosion in Zone I; (**c, d**) pitting corrosion in Zone II, (**e**) IGC in Zone II. Zones I and II are denoted in accordance with Figure 1c. Metallography.

Table 3. Results of the corrosion testing of the welded joints of the PT-3V alloy.

No.	Welding regime				Coarse-grained alloy						UFG alloy					
					HSC test				Tafel test		HSC test				Tafel test	
	T, °C	V_h, °C/min	t, min	P, MPa	HSC character [1] Zone I	HSC character [1] Zone II	h_{max}, μm	h_{av}, μm	i_{corr}, mA/cm²	E_{corr}, mV	HSC character [1] Zone I	HSC character [1] Zone II	h_{max}, μm	h_{av}, μm	i_{corr}, mA/cm²	E_{corr}, mV
0	State before welding					ICC	~600	~400				ICC	~150	~100		
1	600				C	P, ICC	223	162 ± 43	1.21	-471	C	P, ICC	188	124 ± 34	1.03	-486
2	700				C	P, ICC	235	231 ± 39	1.69	-500	-	P, ICC	420	273 ± 62	0.92	-507
3	800	100	10	50	C	P	280	265 ± 48	1.30	-456	C	P, ICC	400	285 ± 59	0.66	-468
4	1030				-	P	358	184 ± 35	1.74	-467						
	1142										C	P, ICC	557	211 ± 45	0.82	-499
5		10			-	P, ICC	238	182 ± 45	1.12	-473	-	P	171	132 ± 24	0.66	-500
6	700	50	10	50	C	P, ICC	235	231 ± 39	1.51	-476	-	P, ICC	442	304 ± 51	1.32	-479
7		100			C	P, ICC	358	185 ± 75	1.69	-500	-	P, ICC	420	273 ± 42	0.92	-507
8		350			C	P, ICC	444	220 ± 92	0.99	-509	-	P, ICC	451	189 ± 36	0.16	-180
9				50	C	P, ICC	290	215 ± 49	0.66	-470	-	P, ICC	430	280 ± 30	0.92	-507
10	700	100	10	70	C	P, ICC	132	108 ± 21	0.69	-495	-	P	138	113 ± 28	1.09	-502
11				100	C	P, ICC	246	178 ± 77	1.04	-495	-	P	163	93 ± 40	1.12	-494
12			0		C	P, ICC	390	211 ± 82	1.24	-475	C	P, ICC	385	249 ± 58	1.77	-507
13	700	100	10	50	C	P, ICC	358	184 ± 75	1.62	-486	-	P, ICC	358	284 ± 55	0.92	-507
14			50		C	P, ICC	354	191 ± 67	1.27	-452	-	P, ICC	495	237 ± 40	1.24	-498
15			90		C	P, ICC	163	125 ± 62	-	-		P, ICC	512	297 ± 47	1.20	-488

[1] P – pitting corrosion, ICC – intercrystalline corrosion, C – crevice corrosion.

The metallographic investigations of the character of the corrosion damage of the specimen surfaces demonstrated a combination of pitting corrosion and the crevice one to take place in the welded joint area in the coarse-grained titanium alloys (Figure 12a,b). The depth of the crevice corrosion defects along the welded joints is determined by the porosity of the joints directly. In the case of highly porous joints obtained in non-optimal regimes of diffusion welding, the depth of corrosion defects may exceed 300 μm. The intensity of the pitting corrosion in the welded joint area depends on the nonuniformity of the microstructure of the coarse-grained alloy in the welded joint area – in a number of cases, a situation when the areas with essentially different microstructure parameters may appear at different sides of the welded joints has been observed (Figure 13). This factor is a consequence, in particular, by a nonuniform distribution of large corrosion pits at different sides of the joint line and an increased uncertainty of measurements of the mean depth of the

Preprints (www.preprints.org) | NOT PEER-REVIEWED | Posted: 27 January 2023 doi:10.20944/preprints202301.0501.v1

corrosion defects (up to 30% of h_{av}, see Table 3). The same factor causes possible nonuniformity of the corrosion of the welded joints. As one can see in Figure 12a,b, the corrosion intensity at one side of the welded joint may differ from the one at another side.

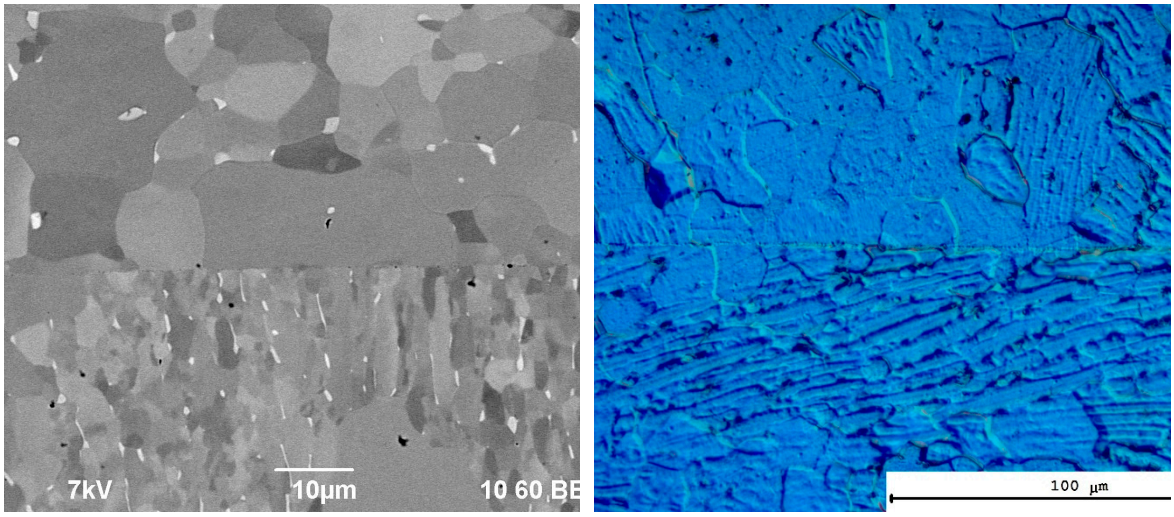

(a) **(b)**

Figure 13. Nonuniformity of the metal microstructure in the weld joint area of the coarse-grained titanium alloy Ti-5Al-2V: (**a**) SEM; (**b**) Metallography.

Outside the welded joints of the coarse-grained titanium alloys, a combination of the intercrystalline corrosion and the pitting corrosion one takes place. The largest corrosion pits were distributed uniformly over the whole specimen area (Figure 12c,d,e; Figure 14). It should be stressed here that the most intensive corrosion fracture was observed in the area of the elongated α-phase grains with increased volume fraction of the β-phase particles (Figure 12c, Figure 14c,d). Note also that the regions of the plate-wise α-phase grains in the coarse-grained specimens were distributed nonuniformly (Figure 3a). This causes a nonuniform character of the corrosion defect distribution over the metal surface.

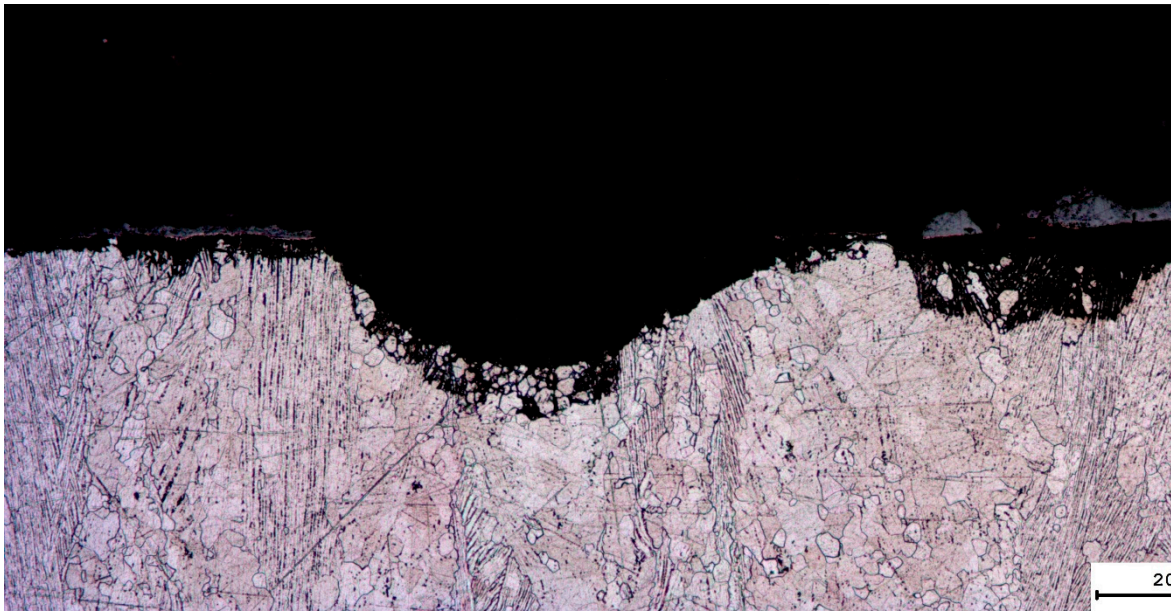

(a)

Preprints (www.preprints.org) | NOT PEER-REVIEWED | Posted: 27 January 2023 doi:10.20944/preprints202301.0501.v1

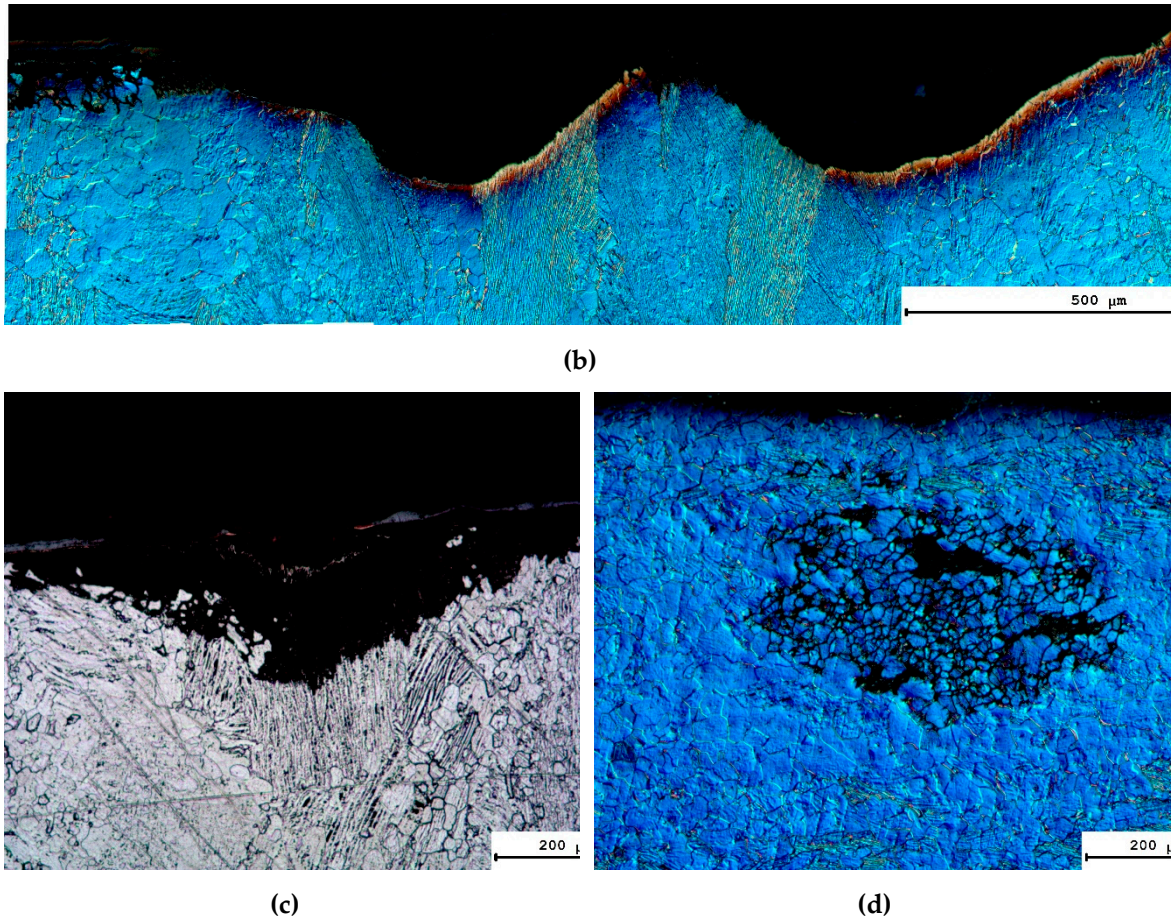

Figure 14. The nonuniform distribution of large corrosion pits at different sides of the joint line of the coarse-grained titanium alloy after HSC testing: (**a**) V_h = 100 °C/min, t = 700 °C, t = 10 min, P = 50 MPa; (**b**) V_h = 100 °C/min, t = 700 °C, t = 10 min, P = 100 MPa. Examples of defect formation in the plate-wise α-phase regions are presented in Figure 14**c**, **d**. Metallography.

The analysis of the character of the corrosion destruction has shown the intercrystalline corrosion to take place at the initial stage. This, in our opinion, is confirmed by the presence of small ICC areas on the specimen surfaces without formation of large corrosion pits (Figure 14d). However, later the ICC defects transform into large corrosion ones defects (Figure 14a,b). The size of the corrosion pits may achieve several hundred microns and was close to typical size of the α-phase elongated grain areas (Figure 3a). This allows suggesting the hot salt corrosion of the coarse-grained specimens to have a two-stage character – at the first stage, the ICC in the fine-grained α-phase elongated grains areas takes place, then the pitting or uniform corrosion at the α-phase equiaxial grains areas, the boundaries of which are practically free of the β-phase inclusions occurs.

The magnitude of the applied stress and the time of the isothermic holding under the pressure affect the depth of the corrosion defects in the welded joints of the coarse-grained specimens the most essentially. As one can see from Table 3, the increasing of the isothermic holding time from 0 up to 90 min (at T = 700 °C, P = 50 MPa) results in the reduction of the corrosion defect depth from 211 ± 42 μm down to 125 ± 53 μm. The maximum corrosion defect depth decreased from 390 μm down to 163 μm. Note that the depth of the corrosion defects varied in a large enough range that results in a large magnitude of the root mean square deviation (i.e. a large uncertainty in the determining of the mean depth of the corrosion defects). As it has been already noted above, this is due to the scatter of the sizes of the plate-wise α-phase regions (Figure 3a) as well as to the cases when the alloys microstructure is different at different sides of the weld joints (Figure 13).

Note also that despite the observed differences in the corrosion resistance of the specimens obtained in different regimes of the diffusion welding, in general, the sizes of the corrosion defects

Preprints (www.preprints.org) | NOT PEER-REVIEWED | Posted: 27 January 2023 doi:10.20944/preprints202301.0501.v1

appeared to be lower than in the Ti-5Al-2V alloy in the initial state (before the diffusion welding) (Table 3).

In the case of the diffusion welding of the UFG alloys, another situation takes place – the crevice corrosion was observed in the case of testing the welded joints with increased porosity only (Table 3, Figure 15a). Outside the welded joints, simultaneous ICC and the pitting one were observed (Figure 15b,c,d) as in the coarse-grained specimens. One can see in Figure 15a how the crevice corrosion region of the welded joint transforms into the ICC one near the weld. The ICC defects and the corrosion pits were distributed nonuniformly on the surface of the welded fine-grained specimen (Figure 15b,c). At present, the origin of the nonequilibrium distribution of the corrosion defects in the UFG specimens is still unclear. Yet, we couldn't relate it unambiguously to the peculiarities of the structure of UFG specimens or of the HSC testing technique.

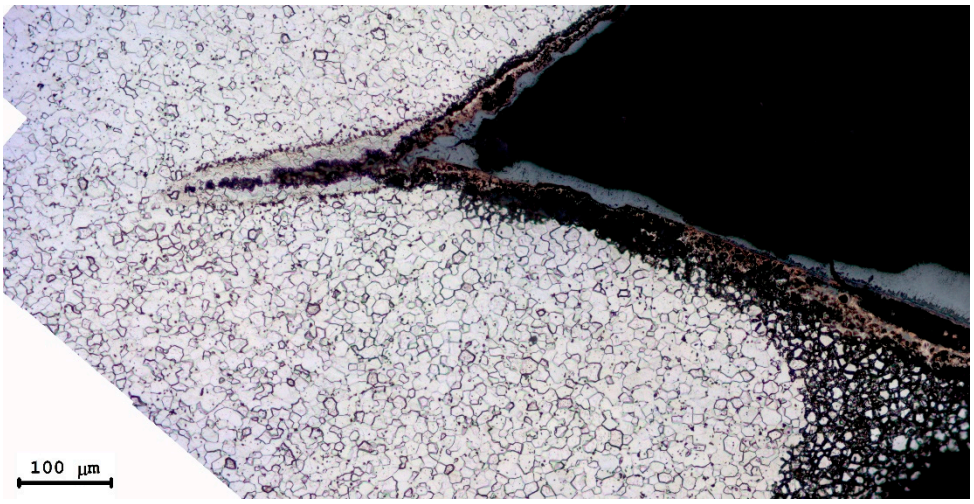

(a)

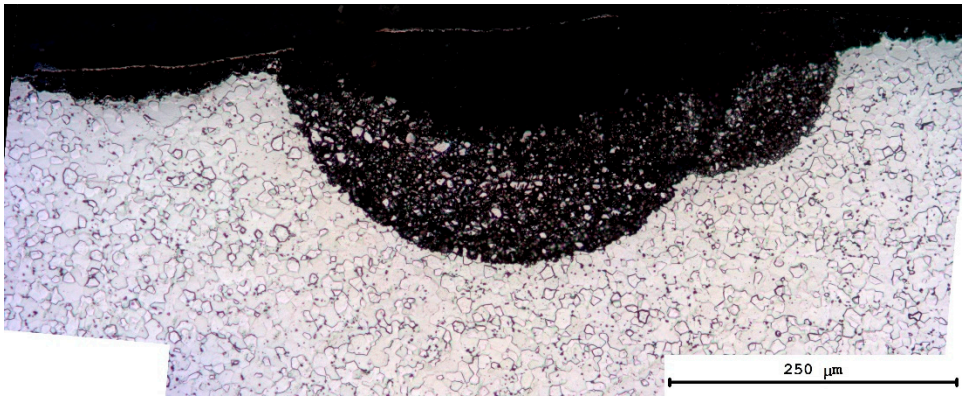

(b)

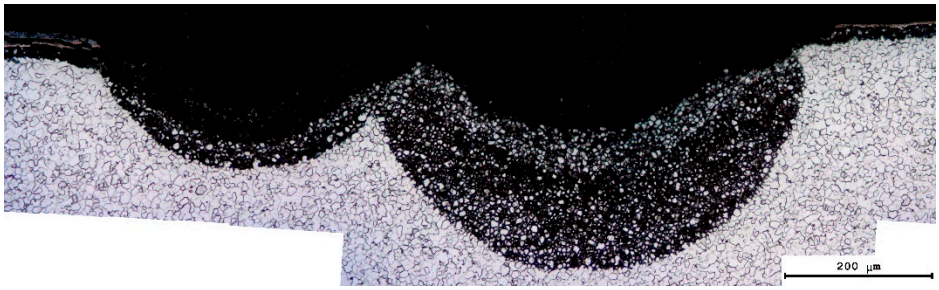

(c)

Preprints (www.preprints.org) | NOT PEER-REVIEWED | Posted: 27 January 2023 doi:10.20944/preprints202301.0501.v1

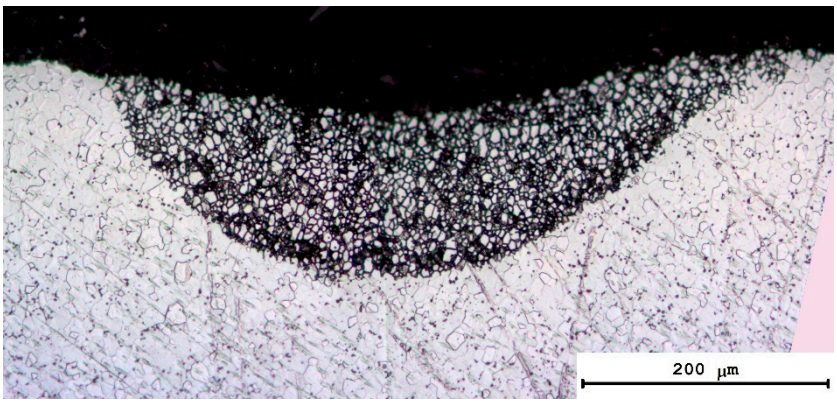

(d)

Figure 15. Corrosion defects on the surface of the UFG specimens of the titanium alloy after HSC testing: (**a**) V_h = 100 °C/min, T = 700 °C, t = 0 min, P = 50 MPa, (**b**) V_h = 100 °C/min, T = 600 °C, t = 10 min, P = 50 MPa, (**c**) V_h = 100 °C/min, t = 800 °C, t = 10 min, P = 50 MPa, (**d**) V_h = 100 °C/min, t = 700 °C, t = 10 min, P = 50 MPa. Metallography.

Note also that the increasing of the holding time and of the diffusion welding temperature resulted in the increasing of the corrosion defect depth in the welded joints of the UFG alloys (Table 3). In the case of low welding temperatures, low heating rates, and low stress, the depth of corrosion defects appeared to be small enough and did not exceed the depths of the ICC defects in the UFG alloy after ECAP (Table 3). To our opinion, the welding regime in the range of moderate heating temperatures (700 °C, corresponding to the two-phase (α+β) region boundary) at small stress (70 MPa), and the heating rate 10 °C/min when the mean depth of the corrosion defects was ~110-130 μm and the large joint defects were absent (i.e. the crevice corrosion was absent) is the optimal one. It should be stressed here that in these regimes the mean pit depth in the UFG specimens appeared to be 1.5-2 times smaller than the depth of the corrosion pits in the coarse-grained specimens (Table 3). So far, one can conclude the welded joints of the UFG alloys to have a higher corrosion resistance as compared to the welded joints of the coarse-grained metals.

The summarizing of the results of the HSC testing shows the increasing of the diffusion welding temperature to result in the increasing of the mean corrosion defect depth (h_{av}) and of the maximum ones (h_{max}) – the increasing of the diffusion welding temperature from 600 °C up to 800 °C resulted in the increasing of the h_{av} from 124 ± 34 μm up to 285 ± 59 μm, the h_{max} increased from 188 μm up to 400–420 μm (Table 3). The increasing of the heating rate from 50 up to 350 °C/min resulted in the reduction of the h_{av} from 304 ± 51 μm down to 189 ± 36 μm. The increasing of the stress applied leads to a decreasing of h_{av} and of the h_{max} in the welded joints of the UFG alloys. The magnitude of the isothermic holding time (t) did not affect the mean size of the corrosion defects essentially in the HSC testing of the welded joint specimens with the fine-grained microstructure (Table 3).

3.5. Electrochemical corrosion test

Now let us analyze the results of the electrochemical investigations of the corrosion resistance of the welded joints presented in Table 3. Tafel curves ln[i] - E had a conventional form (Figure 16). First, note that the testing was performed in 10%HNO_3 + 0.2%HF aqueous solution promoting, first of all, the corrosive destruction of the GBs and the interphase boundaries in the α-titanium alloys [67]. As an example, the SEM images of the welded joints specimens after the electrochemical testing are presented in Figure 17. As one can see in Figure 17, the electrochemical testing resulted in an intense etching of the interphase boundaries near the β-phase particles. When studying the microstructure by SEM in the Z-regime (the atomic number contrast) and MIX-regime, the β-phase particles had a brighter color due to increased concentration of the alloying elements in these ones, first of all – vanadium [26,50]. One can see also that very intensive corrosion etching of the welded joints takes place in the course of the electrochemical testing areas with increased porosity.

Preprints (www.preprints.org) | NOT PEER-REVIEWED | Posted: 27 January 2023 doi:10.20944/preprints202301.0501.v1

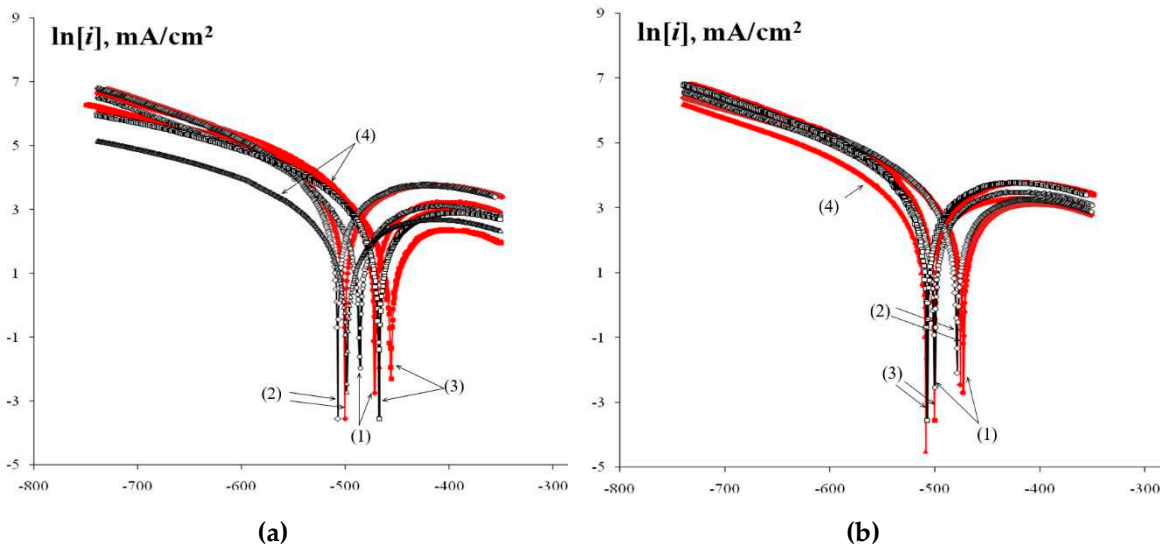

Figure 16. Results of the electrochemical investigations of the coarse-grained (red line) and UFG (black line) titanium alloy specimens: curves ln*i* - E for the (**a**) sintering temperature (circles (line #1) – 600 °C, rhombus (#2) – 700 °C, squares (#3) – 800 °C, triangles (#4) – 1030 °C for the coarse grained alloys; 1140 °C for the UFG alloy); (**b**) heating rate (circles (#1) – 10 °C/min, rhombus (#2) – 50 °C/min, squares (#3) – 100 °C/min, triangles (#4) – 350 °C).

It is worth noting that the corrosion current density i_{corr} in the UFG specimens appeared to be lower than i_{corr} for the welded joints of the coarse-grained specimens whereas the magnitude of the potential E_{corr} was shifted towards more negative values by 10-20 mV. This result evidences indirectly a higher resistance of the specimens with the fine-grained microstructure to the ICC as compared to the coarse-grained alloys.

The summarization of the results presented in Table 3 demonstrated the increasing of the diffusion welding temperature for the UFG alloys from 600 °C up to 800 °C to result in the reduction of the corrosion current density i_{corr} by a factor of ~1.5. The increasing of the heating rate from 50 up to 350 °C/min resulted in the reduction of the corrosion current density from 1.32 μA/cm² down to 0.16 μA/cm². The increasing of the applied stress and of the isothermic holding time did not result in any considerable change of the electrochemical corrosion characteristics of the welded joints in the UFG alloys (Table 3).

In the case of the coarse-grained specimens, no unambiguous dependence of the corrosion current density on main diffusion welding parameters was found. In our opinion, it was caused by the essential nonuniformity of the metal microstructure near the welded joints – as one can see in Figure 13, a situation when fragments with different microstructure types appear in two arbitrary areas of the welded joints occurs frequently enough. The small ranges of the linear Tafel parts of the curves ln[*i*] – E may be the second key factor. This may evidence a significant contribution of chemical dissolving of the GBs when testing the Ti alloys testing in the environment used.

An unambiguous correlation between the results of electrochemical investigations (the magnitude of i_{corr}) and the results of the HSC testing (the magnitudes h_{av}, h_{max}) was absent. This is probably because besides the structural, chemical and phase composition of the GBs, the electrochemical corrosion intensity may be affected additionally by the porosity of the welded joints: the presence of pores would lead to the increasing of the free surface area and to the increasing of the corrosion rate (Figure 17). It was confirmed indirectly by the fact that the i_{corr} for the specimens with high porosity of the joints appeared to be greater than the one for the specimens featured by a small volume fraction of pores in the welded joints. In particular, the i_{corr} for the fine-grained specimens with high porosity of the welded joints (specimens Series #1, 5, 10-12 in Table 3) was ~1.13 mA/cm². This value appeared to be greater than the mean corrosion current density for the fine-grained specimens with low and intermediate porosities of the welded joints (i_{corr} ~ 0.91 mA/cm²).

Preprints (www.preprints.org) | NOT PEER-REVIEWED | Posted: 27 January 2023 doi:10.20944/preprints202301.0501.v1

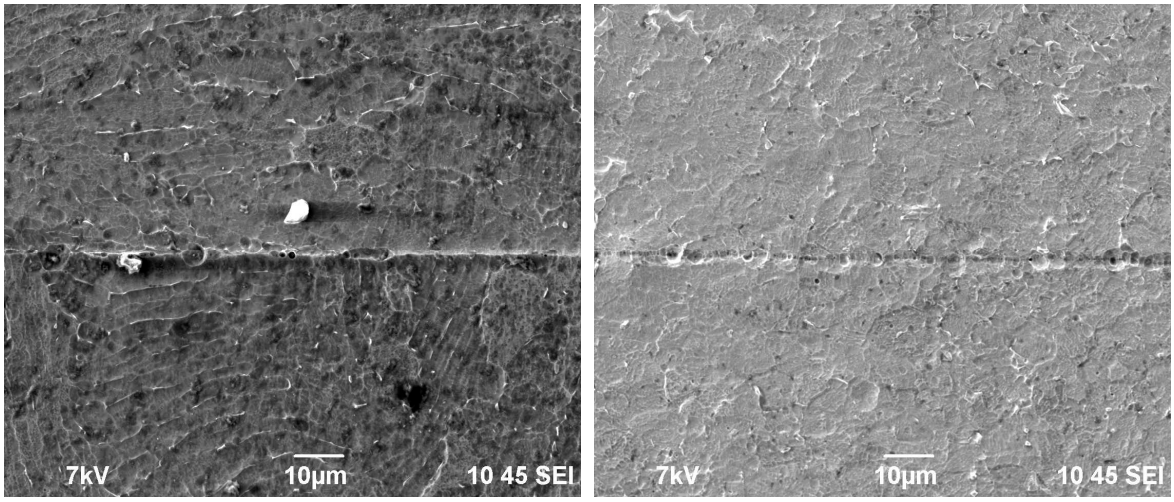

(a) **(b)**

Figure 17. Surfaces of the coarse-grained (**a**) and UFG (**b**) specimens of the titanium alloy (V_h = 100 °C/min, T = 600 °C, t = 10 min, P = 50 MPa) after the electrochemical testing. SEM.

3.6. Microhardness test

The results of microhardness tests (Table 2) demonstrated the diffusion welding regimes not to affect essentially the *Hv* of the welded joints and of the metal outside the joint line in the coarse-grained alloy. The alloy microhardness far away from the junction line was close to the one of the joint material and, as a rule, both these magnitudes were within the range of 2.4-2.6 GPa. Increased values of the *Hv* of the welded joints as compared to the one of Ti-5Al-2V alloy before the diffusion welding (~2.1-2.2 GPa) are related, first of all, to the strain hardening, which the specimens undergo in the course of SPS. This conclusion is confirmed indirectly by a notable increase of the joint *Hv* up to 2.7 GPa in the case of the diffusion welding under the stress of 100 MPa (Table 2).

The *Hv* of the UFG metal inside the welded joints and far away from the joint line exceeded the microhardness of the coarse-grained specimens by ~0.4-0.8 GPa. The highest values of *Hv* ~3.0-3.2 GPa were observed in the specimens obtained by the SPS at low temperatures, high heating rates, or small holding times. The summarization of the obtained results shows the increasing of the heating rate up to 350 °C/min to allow forming the fine-grained microstructure with low porosity and increased hardness (2.9-3.1 GPa) of the welded joints. The increasing of the holding time from 0 up to 90 min (at V_h =100 °C/min, P = 50 MPa, T = 700 °C) resulted in the decreasing of the *Hv* from 2.9 GPa down to 2.5 GPa. The increasing of the stress from 50 MPa up to 100 MPa at 700 °C resulted in an insufficient increasing of the alloy *Hv* from 2.8–2.9 GPa up to 3.0–3.1 GPa but was associated by an intensive plastic deformation of the specimens. In this connection, to our opinion, is the most preferable, the diffusion welding performed by a high-speed heating (350 °C/min) up to the temperature close to the α→β phase transition temperature (700 °C), at the stress 50 MPa, without holding (t = 0 min). This allows ensuring the formation of the fine-grained microstructure simultaneously with increased hardness and corrosion resistance.

4. Discussion

As it has been already noted in Introduction, the HSC is one of the most dangerous fracture processes for the titanium alloys used in nuclear power engineering or in naval aviation. The analysis of the literature data [26,53–55,68] shows the under air access into the test cell HSC in the α- and near-α titanium alloys to have the intercrystalline character preferentially. At given testing conditions (the composition of the medium, the temperatures of testing, availability of the access of oxygen, etc.) the tendency of the α- and near-α titanium alloys to the intercrystalline HSC depends, first of all, on the microstructure, chemical and phase composition of the GBs.

Preprints (www.preprints.org) | NOT PEER-REVIEWED | Posted: 27 January 2023 doi:10.20944/preprints202301.0501.v1

In our case, the most notable effect on the tendency of the near-α alloy Ti-5Al-2V to HSC may cause: (i) the concentration of the corrosion-active alloying elements at the GBs, (ii) the nucleation of the β-phase particles at the GBs as well as (iii) the presence of pores in the welded joints. According to [26,67–69], the formation of the grain boundary segregations of the corrosion active alloying elements, first of all, of vanadium and aluminum [26] as well as the presence of the β-particles containing a high concentration of β-stabilizers (vanadium) [1,2,26,66], may lead to the formation of micro-galvanic couples accelerating the electrochemical corrosion as well as to enhanced corrosion destruction of the GBs. Negative effect of the pores is realized, first of all, via the increasing of the free surface area participating in the chemical or electrochemical reactions. If the HSC testing is conducted under a stress (see [53,54,58–60]), the effect of the pores may be more essential because these ones may play a role of the initiators of the microcrack formation. It can be related, in particular, to the accumulation of the gaseous corrosion reaction products (hydrogen, $TiCl_4$).

Earlier, it was reported also on a possibility of nucleation of α_2-phase nanoparticles and of α''-phase ones during annealing [70] and of the superplastic deformation [71] of the UFG PT-3V (Ti-4.66Al-1.92%V) alloy obtained by Multidirection Forming method (the deformation temperature was 500-800 °C) followed by annealing at 700 °C (1 h). The nanometer-sized particles nucleated inside the α-Ti grains as well as at the GBs and provided an improved stability of the Ti alloy grain microstructure at heating up and deformation [70,71]. During the diffusion welding by SPS, the deformation of the coarse-grained alloy goes via the power-law creep mechanism, in the case of the UFG alloys – via the superplasticity (see [50]). As a consequence, in general, one can expect also the nucleation of the α_2-phase nanoparticles and of the α''-phase ones during the diffusion welding of the Ti alloys by SPS. We think these particles to affect the corrosion resistance of the Ti alloy insufficiently since the sizes and volume fractions of these ones are small and, according to [72], these ones would affect the Ti alloy properties only indirectly affecting the α-Ti grain sizes.

To simplify further analysis, let us assume the plastic deformation of the metal in the course of the diffusion welding to affect the ICC intensity, first of all, by affecting the porosity, microstructure state, and phase composition of the GBs in the alloy.

Let us analyze the effect of the diffusion welding regimes on the resistance of the specimens of the coarse-grained and UFG titanium alloy Ti-5Al-2V to the HSC.

4.1. Corrosion resistance of welded joints. Crevice corrosion

It should be noted in advance that usually α- and near-α Ti alloys intended for nuclear engineering demonstrate a high resistance against the crevice corrosion in the chloride solutions [10,72]. Therefore, the observation of intensive crevice corrosion in the welded joints obtained by diffusion welding was unexpected. According to [72], the crevice corrosion in Ti alloys is modeled usually by testing of a set of Ti plates with Teflon gaskets in highly concentrated aqueous NaCl solution with addition of hydrochloric acid at elevated temperatures. We suppose the rapid crevice corrosion to originate from the formation of an active acidic environment with very low pH in very narrow joint macrodefects. This suggestion corresponds to the staging of chemical reactions going in HSC of Ti alloys. The authors of [54–56] related HSC in Ti alloys to a sequence of the following reactions:

$$TiO_2\ (solid) + 2NaCl\ (solid) + H_2O\ (gas) \rightarrow Na_2TiO_3\ (solid) + 2HCl\ (gas). \quad (1)$$

The oxide film on Ti reacts with the crystalline salts and water with formation of sodium titanate (Na_2TiO_3) and hydrochloride (HCl), which then reacts with Ti with release of atomic hydrogen and gaseous titanium chloride IV ($TiCl_4$):

$$Ti\ (solid) + 4HCl\ (gas) \rightarrow TiCl_4\ (gas) + 4H\ (gas). \quad (2)$$

Hydrogen would be absorbed by the metal at the moment of release that would lead to hydrogenation of the one at the places of the corrosion whereas titanium chloride IV would undergo hydrolysis in the water vapor with formation of hydrochloride and, finally, of titanium oxide (TiO_2) via a number of intermediate products of hydrolysis:

Preprints (www.preprints.org) | NOT PEER-REVIEWED | Posted: 27 January 2023 doi:10.20944/preprints202301.0501.v1

$$TiCl_4\ (gas) + H_2O\ (gas) \rightarrow TiO_2\ (solid) + 4\ HCl\ (gas). \quad (3)$$

Hydrochloride may then react with Ti by reaction (2) with formation titanium chloride IV ($TiCl_4$) and so on. This sequence of reactions explains, in our opinion, the high rate of crevice HSC in the testing of the welded specimens with narrow joint macrodefects.

As it has been already mentioned above, the crevice corrosion took place within the welded joints preferentially. The corrosion rate of the welded joints correlated well with the presence and sizes of the macrodefects and macropores in the welded joints – the higher the porosity of the joints and the greater the initial size of the joint macrodefect in Zone I, the more intensive the crevice HSC. As one can see from Tables 2 and 3, the crevice corrosion in Zone I of the coarse-grained specimens was observed in the corrosion tests of the specimens with high weld porosity. In the coarse-grained specimens in Series #4 and #5 featured by low porosity, the crevice corrosion was almost absent (the depths of the corrosion defects were small and didn't exceed 10-20 μm).

In general, similar situation takes place in the testing of the UFG specimens – the cervix corrosion was observed in the specimens in Series #1, #3, and #12 with high weld porosity. It is interesting to note that in the UFG specimens in Series #10 and #11 obtained at increased stress, no traces of crevice corrosion were found. Probably, the absence of the crevice corrosion traces in these specimens is because the porosity in these ones arouse preferentially due to the formation of isolated macropores owing to intense plastic deformation, not to the formation of macrodefects of the joints. The presence of the crevice corrosion in the specimens in Series #4 obtained by welding in the β-region is probably due to the flattening of the specimen at its deformation at 1142 °C. This leads to arising of strong tensile strain along the weld line and, hence, to the fracture of the weld and to the formation of new joint macrodefects in this one (Figure 1c).

It allows concluding the joint macrodefects, not the isolated macropores to be the most dangerous type of defects in the scope of the crevice corrosion development in the specified conditions of high-temperature testing in the crystal salt mixture. Small sizes of the joint macrodefects and smaller volume fraction of the macropores in the UFG alloys (Figure 6) provide a higher resistance of these ones against the crevice corrosion as compared to the coarse-grained specimens. The origin of accelerated diffusion weldability in the UFG alloy as compared to the coarse-grained specimens was described in [50]. In addition, it is worth noting that in order to ensure high resistance of the welded joints against the crevice corrosion, it is more reasonable to perform the diffusion welding in the molds limiting the plastic deformation of the Ti alloys at elevated temperatures. This allows minimizing the negative effect of the tensile strain acting along the weld line and arising at the loss of the shape stability of the specimens but may lead to the carbonization of the surface layers of the Ti specimens [53,73,74].

4.2. Corrosion resistance of the metal. Pitting and intercrystalline corrosion

Let us analyze now the corrosion resistance of the metal far away from the welding area. As it has been already shown in Results section, far away from the welded joint line, the corrosion destruction goes via the intercrystalline corrosion mechanism preferentially. This allows suggesting the structure, chemical and phase composition of the GBs in the Ti alloy to affect the corrosion resistance of the metal mostly.

First, let us analyze the effect of the welding temperature on the corrosion resistance of the welded coarse-grained and UFG specimens (specimens in Series #1-4 in Tables 2 and 3).

Note that after heating with the rate V_h = 100 °C/min up to the temperature 600 °C and holding during 10 min at 50 MPa, the h_{av} reduced from 400-600 μm (Series #0) down to 162 ± 43 μm (Series #1) and the corrosion resistance of the coarse-grained alloy became close to the one of the UFG alloy (Table 3). This evidences the improvement of the corrosion resistance of the coarse-grained titanium alloy Ti-5Al-2V by heating. Since no essential changes of the grain sizes and of the volume fraction of the β-phase particles takes place at such a treatment (Table 2), the decreasing of the local concentration of vanadium at the titanium GBs, is the most probable origin of increased corrosion resistance. This, in our opinion, originates from the diffusion equalization of the local V concentration

Preprints (www.preprints.org) | NOT PEER-REVIEWED | Posted: 27 January 2023 doi:10.20944/preprints202301.0501.v1

between the GBs enriched with V and the depleted ones. It takes place probably because of action of Fick's law resulting in the reduction of the difference in V concentrations between the I-type GBs and the II-type ones in the Ti alloy. The plastic deformation of the Ti alloy may be an additional possible origin of accelerated diffusion mass transfer.

As one can see form Table 3, further increasing of the welding temperature of the coarse-grained alloy resulted in a slight decreasing of the h_{av}.

The structural investigations demonstrated the mean size of the equiaxial grains of α-phase and the structural-phase state of the GBs of these ones almost not to change in the course of heating the coarse-grained Ti-5Al-2V alloy. However, an inessential increasing of the elongated α-phase grain sizes and, the most important, the increasing of the sizes and volume fraction of the β-phase particles was observed (Table 2). The most clearly this was expressed after welding at 800 °C corresponding to the two-phase (α+β) region. This result agrees well with the data reported in [14,75,76] where the annealing in the intermediate (α+β)-region was demonstrated to result in the increasing of the β-phase particle sizes with simultaneous decreasing of the vanadium concentration in GBs. It favored the reduction of the ICC intensity in the coarse-grained specimens.

As one can see form Table 3, the effect of the heating temperature on the corrosion resistance of the UFG alloys had another character – the increasing of the welding temperature resulted in an increasing of the depth of the corrosion defects.

As it has been shown above, the microstructure of the UFG alloy Ti-5Al-2V in the initial state was close enough to the microstructure of pure titanium (the grain boundary vanadium segregations and the large β-phase particles were absent). However, it is worth noting that the recrystallization start in the UFG alloy Ti-5Al-2V when heating at 500-550 °C (see [26,50]). An fast GB migration may result in the increasing of the local concentration of the vanadium at the GBs. (The distribution coefficient of vanadium in titanium is ~0.801 [77]; hence (see [13]), vanadium is a horophilic alloying element in titanium). This factor is one of the main origins of the decreasing of the corrosion resistance of the UFG alloys with increasing temperature (Table 2). In the case of increasing the welding temperature up to (α+β)-region boundary, the formation and growth of the β-particles may be an additional factor promoting the decreasing of the corrosion resistance of the UFG alloys.

Now, let us analyze the effect of the holding time on the corrosion resistance of the Ti alloy (specimens in Series #12-15 in Table 3). The welding was performed at 700 °C, near the (α+β)-region boundary.

As one can see from Table 3, the increasing of the diffusion welding time from 0 min up to 90 min resulted in the decreasing of the h_{av} and h_{max} in the coarse-grained specimens. Note that the isothermic holding at this temperature resulted in a partial dissolving of the β-particles (Table 2). Since the β-particles contain an increased V concentration, the presence of these ones at the GBs causes the formation of the microgalvanic pairs provoking the ICC. In the case of decreasing of the volume fraction of these ones (that has been observed when increasing the isothermic holding time at 700 °C), one should expect an increasing of the corrosion resistance of the coarse-grained alloy.

As one can see from Table 3, the increasing of the welding time of the UFG specimens resulted in an increasing of the depth of the corrosion defects. Note that the increasing of the holding time at 700 °C would also result in more intensive grain growth (Table 2) and, hence, in increasing the concentration of the vanadium at the migrating GBs. This would result in the increasing of the depth of the ICC defects that has been observed in the experiment (Table 3).

The increasing of the heating rate didn't affect the corrosion resistance of the coarse-grained specimens (Series #5-8) essentially but leads to a nonmonotonous variation of the depth of the corrosion defects in the UFG alloy (Table 3).

The decreasing of the corrosion defect sizes in the UFG alloys with increasing heating rate may be explained in the same way – the decreasing of the heating duration would result in the reduction of the grain growth intensity (Table 2) and in the reduction of the harmful element concentration at the GBs. This should result in a decreasing of the depth of the corrosion defects at high heating rates. At low heating rates (V_h = 10 °C/min), the pitting corrosion only has been observed in the welded

Preprints (www.preprints.org) | NOT PEER-REVIEWED | Posted: 27 January 2023 doi:10.20944/preprints202301.0501.v1

UFG specimens (Table 3, Series #5) that didn't allow comparing correctly the specimens obtained at high and low heating rates.

The microstructure analysis demonstrated the volume fraction of the nucleated β-phase particles to be large enough (Table 3). However, it did not result in an essential reduction of the corrosion resistance of the alloy – the mean depth of the ICC defects in the coarse-grained welded specimen was ~184 ± 35 μm, in the UFG specimen it was 211 ± 45 μm (Table 3). In our opinion, it is related to the disappearing of the grain boundary segregations of vanadium after heating up to the β-region whereas the nucleated β-particles contain a lower concentration of the vanadium that coincides well to [14,75,76,78].

Note also that the suggestion on the role of V in HSC of Ti alloys agrees well with the results of XRD phase analysis. As it was shown above, various V-based phases ($VO_{1.15}$, $V_2Ti_3O_9$, Al_3V) were found in the corrosion products on the surfaces of the specimens welded at low and moderate temperatures. According to the XRD phase analysis, the Al-based phases (in the presence of vanadium oxides) dominated in the HSC products of the specimens welded at elevated temperatures in the β-region instead of the V-based phases. This, in our opinion, agrees with the suggestion the control of the grain boundary segregations of V and of the content of the β-phase particles with increased V concentration in the welded specimens of Ti-5Al-2V alloy to play an important role in ensuring high resistance to HSC.

5. Conclusions

1. The effect of the regimes of high-speed diffusion welding by SPS on the density and microstructure of the near-α titanium alloy Ti-5Al-2V (Russian industrial grade PT-3V) has been investigated. The UFG specimens have been shown to have a higher weldability as compared to the coarse-grained alloys, in the welded joints of which the macrodefects and micropores provoking the crevice corrosion were observed. In the UFG specimens, the joint macrodefects were absent practically, the volume fractions of the macro- and micropores were very small that provides a high resistance of the welded joints to the crevice corrosion.

2. The corrosion resistance of the coarse-grained Ti-5Al-2V alloy specimens after the diffusion welding was shown to exceed the corrosion resistance of the alloy in the initial state. Outside of the welded joints, the HSC of the coarse-grained specimens goes by the intercrystalline and pitting corrosion mechanisms. The corrosion defects were distributed over the surfaces of coarse-grained specimens nonuniformly and were concentrated mainly in the fine-grained elongated α-phase area, at the grain boundaries of which an increased volume fraction of the β-phase particles was observed. The HSC of the coarse-grained specimens has a two-stage character – at the first stage, the intercrystalline corrosion is developing, which then transforms into the pitting corrosion.

3. The corrosion resistance of the UFG alloy Ti-5Al-2V was found to depend mainly on the concentration of the corrosion-active alloying elements (vanadium) at the titanium grain boundaries. The increasing of the local concentration of vanadium on the migrating grain boundaries in the titanium alloy with increasing temperature and diffusion welding time affects the resistance against the HSC negatively. The diffusion welding performed by the temperature close to the α→β phase transition boundary (700 °C) at the stress 50 MPa without holding (t = 10 min) was shown to be the most preferable. It allows ensuring the formation of the fine-grained microstructure with simultaneously increased hardness and corrosion resistance.

Author Contributions: Conceptualization, V.N.C. and A.V.N.; methodology, V.N.C. and A.V.N.; formal analysis, V.N.C. and A.V.N.; investigation, C.V.L., V.I.K., P.V.A., M.S.B., N.Y.T., A.I.M.; resources, V.N.C.; data curation, A.V.N.; writing—original draft preparation, V.N.C. and A.V.N.; writing—review and editing, V.N.C. and A.V.N.; visualization, A.V.N.; supervision, V.N.C.; project administration, V.N.C.; funding acquisition, V.N.C. All authors have read and agreed to the published version of the manuscript.

Funding: This research was funded by Ministry of Science and Higher Education of the Russian Federation, grant number H-498-99_2021-2023 (075-15-2021-1332) of Federal academic leadership program Priority 2030. The investigations of the microstructure of the alloys by TEM were carried out using the instrumentation of the Center Collective Use "Materials Science and Metallurgy" (National University of Science and Technology

"MISIS") supported by Ministry of Science and Higher Education of the Russian Federation (grant No. 075-15-2021-696).

Data Availability Statement: Not applicable.

Acknowledgments: The authors are grateful to D.A. Gudz' for assistance in the XRD experiments. The authors are also grateful to M.M. Vostokov for assistance in preparing the samples for investigations.

Conflicts of Interest: The authors declare no conflict of interest.

Abbreviations: CG—coarse-grained (alloy); ECAP—Equal Channel Angular Pressing; ICC—intercrystalline corrosion; GB—grain boundary; HSC—hot salt corrosion; RT—room temperature; SEM—scanning electron microscopy; SPD—Severe Plastic Deformation; SPS—Spark Plasma Sintering; TEM—transmission electron microscopy; UFG—ultrafine-grained (alloy); XRD—X-ray diffraction (phase analysis).

References

1. Lütjering, G.; Williams, J.C. *Titanium*, 2nd ed.; Springer: Berlin Heidelberg, Germany, 2007; p. 442.
2. Jafee, R.I.; Burte, H.M. (Eds.). *Titanium Science and Technology*. Springer: New York, US, 1973; p. 2739.
3. Gorynin, I.V.; Chechulin, B.B. *Titan in Mechanical Engineering*. Mashinostroenie: Moscow, Russia, 1990; p. 400. (in Russian).
4. Bilobrov, I.; Trachevsky, V. Approach to modify the properties of titanium alloys for use in nuclear industry. *J. Nucl. Mater.* **2011**, *415*, 222-225. doi:10.1016/j.jnucmat.2011.05.056
5. Oryshchenko, A.S.; Gorynin, I.V.; Leonov, V.P. et al. Marine titanium alloys: Present and future. *Inorg. Mater. Appl. Res.* **2015**, *6*, 571-579. doi:10.1134/S2075113315060106
6. Leonov, V.P.; Gorynin, I.V.; Kudryavtsev, A.S. et al. Titanium alloys in steam turbine construction. *Inorg. Mater. Appl. Res.* **2015**, *6*, 580-590. doi:10.1134/S2075113315060076
7. Gorynin, I.V. Titanium alloys for marine application. *Mater. Sci. Eng. A.* **1999**, *263*, 112-116. doi:10.1016/S0921-5093(98)01180-0
8. Leonov, V.P.; Chudakov, E.V.; Malinkina, Y.Y. The influence of microadditives of ruthenium on the structure, corrosive-mechanical strength, and fractography of destruction of pseudo-alpha-titanium alloys. *Inorg. Mater. Appl. Res.* **2017**, *8*, 556-565. doi:10.1134/S2075113317040165
9. Kozhevnikov, O.A.; Nesterova, E.V.; Rybin, V.V.; Yarmolovich, I.I. Influence of neutron irradiation of deformability and fracture micromechanisms of titanium α-alloys. *J. Nucl. Mater.* **1999**, *271-272*, 472-477. doi:10.1016/S0022-3115(98)00803-4
10. Malinkina, Y.Y.; Chudakov, E.V.; Leonov, V.P. The influence of ruthenium on structure, corrosion and mechanical properties, and fatigue characteristics of titanium α-alloys in corrosive environment. *Inorg. Mater. Appl. Res.* **2017**, *8*, 906-913. doi:10.1134/S2075113317060090
11. Murashov, A.A.; Berendeyev, N.N.; Nokhrin, A.V.; Galaeva, E.A.; Chuvil'deev, V.N. Investigation of the process of fatigue and corrosion-fatigue destruction of pseudo-α titanium alloy. *Inorg. Mater. Appl. Res.* **2022**, *13*, 349-356. doi:10.1134/S2075113322050318
12. Segal, V. Review: Modes and Processes of Severe Plastic Deformation. *Materials* **2018**, *11*, 1175. doi:10.3390/ma11071175
13. Segal, V.M.; Beyerlein, I.J.; Tome, C.N.; Chuvil'deev, V.N.; Kopylov, V.I. *Fundamentals and Engineering of Severe Plastic Deformation*. Nova Science Publishers: New York, USA, 2010; p. 542.
14. Gornakova, A.S.; Straumal, A.B.; Khodos, I.I. et al. Effect of composition, annealing temperature, and high pressure torsion on structure and hardness of Ti-V and Ti-V-Al alloys. *J. Appl. Phys.* **2019**, *125*, 082522. doi:10.1063/1.5053937
15. Straumal, B.B.; Kilmametov, A.R.; Ivanisenko, Y. et al. Diffusive and displacive phase transitions in Ti-Fe and Ti-Co alloys under high pressure torsion. *J. Alloys Compd.* **2018**, *735*, 2281-2286. doi:10.1016/j.jallcom.2017.11.317
16. Alkazraji, H.; El-Danaf, E.; Wolfmann, M.; Wagner, L. Enhanced fatigue strength of commercially pure Ti processed by rotary swaging. *Adv. Mater. Sci. Eng.* **2015**, *2015*, 301837. doi:10.1155/2015/301837
17. Pachla, W.; Kulczyk, M.; Prybysz, S. et al. Effect of severe plastic deformation realized by hydrostatic extrusion and rotary swaging on the properties of CP Ti grade 2. *J. Mater. Process. Techn.* **2015**, *221*, 255-268. doi:10.1016/j.jmatprotec.2015.02.027

18. Zherebtsov, S.; Kudryavtsev, E.; Kostjuchenko, S. et al. Strength and ductility-related properties of ultrafine grained two-phase titanium alloy produced by warm multiaxial forging. *Mater. Sci. Eng. A.* **2012**, *536*, 190-196. doi:10.1016/j.msea.2011.12.102
19. Zherebtsov, S.V.; Kudryavtsev, E.A.; Salishchev, G.A. et al. Microstructure evolution and mechanical behavior of ultrafine Ti-6Al-4V during low-temperature superplastic deformation. *Acta Mater.* **2016**, *121*, 152-163.doi:10.1016/j.actamat.2016.09.003
20. Czervinski, A.; Lapovok, R.; Tomus, D.; Estrin, Y.; Vinogradov, A. The influence of temporary hydrogenation on ECAP formability and low cycle fatigue life of CP titanium. *J. Alloys Compd.* **2011**, *509*, 2709-2715. doi:10.1016/j.jallcom.2010.11.188
21. Estrin, Y.; Vinogradov, A. Fatigue behavior of light alloys with ultrafine grain structure produced by severe plastic deformation: An overview. *Int. J. Fatigue* **2010**, *32*, 898-907. doi:10.1016/j.ijfatigue.2009.06.022
22. Vinogradov, A.Yu.; Stolyarov, V.V.; Hashimoto, S.; Valiev, R.Z. Cyclic behavior of ultrafine-grain titanium processed by severe plastic deformation. *Mater. Sci. Eng. A.* **2001**, *318*, 163-173.doi:10.1016/S0921-5093(01)01262-X
23. Kral, P.; Dvorak, J.; Zherebtsov, S. et al. Effect of severe plastic deformation on creep behaviour of a Ti-6Al-4V alloy. *J. Mater. Sci.* **2013**, *48*, 4789-4795. doi:10.1007/s10853-013-7160-9
24. Kral, P.; Dvorak, J.; Blum, W. et al. Creep study of mechanisms involved in low-temperature superplasticity of UFG Ti-6Al-4V processed by SPD. *Mater. Charact.* **2016**, *116*, 84-90. doi:10.1016/j.matchar.2016.04.007
25. Balyanov, A.; Kutnyakova, J.; Amirkhanova, N.A. et al. Corrosion resistance of ultrafine-grained Ti. *Scr. Mat.* **2004**, *51*, 225-229. doi:10.1016/j.scriptamat.2004.04.011
26. Chuvil'deev, V.N.; Kopylov, V.I.; Nokhrin, A.V. et al., Study of mechanical properties and corrosive resistance of ultrafine-grained α-titanium alloy Ti-5Al-2V. *J. Alloys Compd.* **2017**, *723*, 354-367. doi:10.1016/j.jallcom.2017.06.220
27. Mosleh, A.O.; Mikhaylovskaya, A.V.; Kotov, A.D. et al. Superplastic deformation behavior of ultra-fine-grained Ti-1V-4Al-3Mo alloy: Constitutive modeling and processing map. *Mater. Res. Expr.* **2019**, *6*, 096584. doi:10.1088/2053-1591/ab31f9
28. Raltson, K.; Birbilis, N. Effect of grain size on corrosion: A review. *Corrosion* **2010**, *66*, 0750051-07500513. doi:10.5006/1.3462912
29. Gu, Y.; Ma, A.; Jiang, J. et al. Simultaneously improving mechanical properties and corrosion resistance of pure Ti by continuous ECAP plus short-duration annealing. *Mater. Charact.* 2018, 138, 38-47. doi:10.1016/j.matchar.2018.01.050
30. Fattah-alhosseini, A.; Imantalab, O.; Ansari, G. The role of grain refinement and film formation potential on the electrochemical behavior of commercial pure titanium in Hank's physiological solution. *Mater. Sci. Eng. C.* **2017**, *71*, 827-834. doi:10.1016/j.msec.2016.10.072
31. Chojnaka, A.; Kawalko, J.; Koscielny, H. et al. Corrosion anisotropy of titanium deformed by the hydrostatic extrusion. *Appl. Surf. Sci.* **2017**, *426*, 987-994. doi:10.1016/j.apsusc.2017.07.231
32. Kim, H.S.; Kim, W.J. Annealing effects on the corrosion resistance of ultrafine-grained pure titanium. *Cor. Sci.* **2014**, *89*, 331-337. doi:10.1016/j.corsci.2014.08.017
33. Kim, H.S.; Yoo, S.J.; Ahn, J.W. et al. Ultrafine grained titanium sheets with high strength and high corrosion resistance. *Mater. Sci. Eng. A.* **2011**, *528*, 8479-8485. doi:10.1016/j.msea.2011.07.074
34. Gurao, N.P.; Manivasagam, G.; Govindaraj, P. et al. Effect of texture and grain size on bio-corrosion response of ultrafine-grained titanium. *Metall. Mater. Trans. A* **2013**, *44*, 5602-5610. doi:10.1007/s11661-013-1910-9
35. Korshunov, A.V.; Il'in, A.P.; Lotkov, A.I. et al. Reactivity of submicrocrystalline titanium: I. Regulation of oxidation when heated in air. *Inorg. Mater. Appl. Res.* 4 (2012) 5-12. (in Russian).
36. Bozhko, P.V.; Korshunov, A.V.; Il'in, A.P. et al. Reactivity of submicrocrystalline titanium: II. Electrochemical properties and corrosion stability in sulfuric acid solutions. *Inorg. Mater. Appl. Res.* **2013**, *4*, 85-91. doi:10.1134/S2075113313020032
37. Topol's'kyi, V.P.; Petrychenko, I.K.; Akhonin, S.V.; Mishchenko, R.M. Weldability of T110 high-strength titanium alloy. *Mater. Sci.* **2008**, *44*, 413-417. doi:10.1007/s11003-008-9098-7
38. Lukoyanov, A.V. Formation of pores in the weld metal in automatic argon-shielded arc welding of titanium alloys. *Welding Int.* **2014**, *28*, 301-303. doi:10.1080/09507116.2013.796682
39. Gao, F.; Li, P.; Jiang, P.; Liao, Z. The effect of constraint conditions on microstructure and properties of titanium alloy electron beam welding. *Mater. Sci. Eng. A* **2018**, *721*, 117-124. doi:10.1016/j.msea.2018.02.069

40. Su, M.-L.; Li, J.-N.; Liu, K.-G. et al. Mechanical property and characterization of TA1 titanium alloy sheets welded by vacuum electron beam welding. *Vacuum* **2019**, *159*, 315-318. doi:10.1016/j.vacuum.2018.10.027
41. Mironov, S.; Sato, Y.S.; Kokawa, H. Friction-stir welding and processing of Ti-6Al-4V titanium alloy: A review. *J. Mater. Sci. Techn.* **2018**, *34*, 58-72. doi:10.1016/j.jmst.2017.10.018
42. Meng, X.; Huang, Y.; Cao, J. et al. Recent progress on control strategies for inherent issues in friction stir welding. *Progr. Mater. Sci.* **2021**, *115*, 100706. doi:10.1016/j.pmatsci.2020.100706
43. Medvedev, A.Yu.; Bychkov, V.M.; Selivanov, A.S. et al. Linear friction welding of two-phase titanium alloys VT6 and VT8-1. *Welding Int.* **2015**, *29*, 66-69. doi:10.1080/09507116.2014.888191
44. Nasresfahani, A.R.; Soltanipur, A.R.; Farmanesh, K.; Ghasemi, A. The effect of friction stir welding on corrosion behavior of Ti-6Al-4V. *J. Mater. Eng. Performance.* **2017**, *26*, 4311-4318. doi:10.1007/s11665-017-2917-y
45. Olevsky, E.; Dudina, D. *Field-Assisted Sintering;* Springer: Basel, Switzerland, 2018; p. 425. doi:10.1007/978-3-319-76032-2
46. Tokita, M. Spark Plasma Sintering (SPS) Method, Systems, and Applications. in *Handbook of Advanced Ceramics*, 2nd ed.; Somiya, S. Ed.; Academic Press: London, UK. 2013; p. 1149-1177. doi:10.1016/B978-0-12-385469-8.00060-5
47. Hulbert, D.M.; Anders, A.; Dudina, D.V. et al. The absence of plasma in "spark plasma sintering". *J. Appl. Phys.* **2008**, *104*, 033305. doi:10.1063/1.2963701
48. Ozerov, M.; Klimova, M.; Sokolovsky, V. et al. Evolution of microstructure and mechanical properties of Ti/TiB metal-matrix composite during isothermal multiaxial forging. *J. Alloys Compd.* **2019**, *770*, 840-848. doi:10.1016/j.jallcom.2018.08.215
49. Weston, N.S.; Derguti, F.; Tudball, A.; Jackson, M. Spark plasma sintering of commercial and development titanium alloys powders. *J. Mater. Sci.* **2015**, *50*, 4860-4878. doi:10.1007/s10853-015-9029-6
50. Chuvil'deev, V.N.; Nokhrin, A.V.; Kopylov, V.I. et al. Spark plasma sintering for high-speed diffusion bonding of the ultrafine-grained near-α Ti-5Al-2V alloy with high strength and corrosion resistance for nuclear engineering. *J. Mater. Sci.* **2019**, *54*, 14926-14949. doi:10.1007/s10853-019-03926-6
51. Yang, J.; Wang, G.; Jiao, X. et al. Current-assisted diffusion bonding of extruded Ti-22Al-25Nb alloy by Spark Plasma Sintering: Interfacial microstructure and mechanical properties. *J. Mater. Engin. Performance.* **2018**, *27*, 3035-3043. doi:10.1007/s11665-018-3398-3
52. Zhao, Z.; Wang, G.; Zhang, Y. et al. Fast recrystallization and phase transformation in ECAP deformed Ti-6Al-4V alloy induced by pulsed electric current. *J. Alloys Compd.* **2019**, *786*, 733-741. doi:10.1016/j.jallcom.2019.01.328
53. Nokhrin, A.; Andreev, P.; Boldin, M.; Chuvil'deev, V.; Chegurov, M.; Smetanina, K.; Gryaznov, M.; Shotin, S.; Nazarov, A.; Shcherbak, G.; Murashov, A.; Nagicheva, G. Investigation of microstructure and corrosion resistance of Ti-Al-V titanium alloys obtained by Spark Plasma Sintering. *Metals* **2021**, *11*, 945. doi:10.3390/met11060945
54. Chevrot, Th. Pressure effects on the holt-salt stress-corrosion cracking of titanium alloys. PhD Thesis. Cranfield University. School of Industrial and Manufacturing Science, Bedford, UK, 1994. https://dspace.lib.cranfield.ac.uk/handle/1826/7745
55. Sinigaglia, D.; Taccani, G.; Vicentini, B. Hot-salt-stress-corrosion cracking of titanium alloys. *Cor. Sci.* **1998**, *18*, 781-796. doi:10.1016/0010-938X(78)90015-X
56. Pustode, M.D.; Raja, V.S.; Paulose, N. The stress-corrosion cracking suspeptibility of near-α titanium alloy IMI 834 in presence of hot salt. *Cor. Sci*. **2014**, *82*, 191-196. doi:10.1016/j.corsci.2014.01.013
57. Ciszaka, C.; Popa, I.; Brossard, J.-M. et al. NaCl induced corrosion of Ti-6Al-4V alloy at high temperature. *Cor. Sci*. **2016**, *110*, 91-104. doi:10.1016/j.corsci.2016.04.016
58. Myers, J.R.; Hall, J.A. Hat salt corrosion cracking of titanium alloys: An improved model for the mechanism. *Corrosion* **1977**, *33*, 252-257. doi:10.5006/0010-9312-33.7.252
59. Pustode, M.D.; Raja, V.S. Hot salt stress corrosion cracking behavior of Ti-6242S alloy. *Metall. Mater. Trans. A* **2015**, *46*, 6081-6089. doi:10.1007/s11661-015-3155-2
60. Pustode, M.D.; Raja, V.S.; Dewangan, B.; Paulose, N. Effect of long term exposure and hydrogen effects on HSSCC behaviour of titanium alloy IMI 834. *Mater. Des*. **2015**, *86*, 841-847. doi:10.1016/j.matdes.2015.08.002
61. Joseph, S.; Lindley, T.C.; Dye, D.; Saunders, E.A. The mechanisms of hot salt stress corrosion cracking in titanium alloy Ti-6Al-2Sn-4Zr-6Mo. *Cor. Sci*. **2018**, *134*, 169-178. doi:10.1016/j.corsci.2018.02.025

62. Pyshmintsev, I.Yu.; Kosmatskii, Ya.I.; Filyaeva, E.A. et al. Alloy Ti-3Al-2.5V hot-extruded pipe metal structure and properties. *Metallurgist* **2018**, *62*, 374-379. doi:10.1007/s11015-018-0671-5
63. Illarionov, A.G.; Kostamatskii, Ya.I.; Filyaeva, E.A. et al. Experimental determination of temperature parameters for evaluating the possibility of manufacturing alloy Ti-3Al-2.5V hot-extruded tubes. *Metallurgist* **2017**, *60*, 983-988. doi:10.1007/s11015-017-0396-x
64. Illarionov, A.G.; Vodolazskiy, F.V.; Barannikova, N.A. et al. Influence of phase composition on thermal expansion of Ti-0.4Al, Ti-2.2Al-2.5Zr and Ti-3Al-2.5V alloys. *J. Alloys Compd.* **2021**, *857*, 158049. doi:10.1016/j.jallcom.2020.158049
65. Bykh, O.; Bakhmetev, A.; Sandler, N. et al. Hot-salt corrosion of alloys PT-7M, 42XHM, Inconel 690 and Incoloy 800. *Applied Solid State Chemistry* **2019**, *1*, 23-31. doi:10.18572/2619-0141-2019-1-23-31
66. Andreev, P.V.; Gudz, D.A.; Smetanina, K.E. Surface treatment of titanium alloys for the X-ray diffraction study. *AIP Conf. Proc.* **2020**, *2315*, 03001. doi:10.1063/5.0036642
67. Chuvil'deev, V.N.; Kopylov, V.I.; Nokhrin, A.V. et al. Effect of severe plastic deformation realized by rotary swaging on the mechanical properties and corrosion resistance of near-α-titanium alloy Ti-2.5Al-2.6Zr. *J. Alloys Compd.* **2019**, *785*, 1233-1244. doi:10.1016/j.jallcom.2019.01.268
68. Tomashov, N.D.; Chernova, G.P. *Theory of corrosion and corrosion-resistant structural alloys*. Metallurgiya: Moscow, Russia, 1986; 358 p. (in Russian).
69. Tavadze, F.N.; Mandzhgaladze, S.N. *Corrosion resistance of titanium alloys.* Metallurgiya: Moscow, Russia, 1969; 208 p. (in Russian).
70. Tomashov, N.D. *Titanium and Titanium-based corrosion-resistance alloys*. Metallurgiya: Moscow, Russia, 1985; 80 p. (in Russian).
71. Ratochka, I.V.; Lykova, O.N.; Naydenkin, E.V. Influence of low-temperature annealing time on the evolution of the structure and mechanical properties of a titanium Ti-Al-V alloy in the submicrocrystalline state. *Phys. Metals Metallogr.* **2015**, *116*, 302-308. doi:10.1134/S0031918X15030114
72. Ratochka, I.; Lykova, O.; Mishin, I.; Naydenkin, E. Superplastic deformation behavior of Ti-4Al-2V alloy governed by its structure and precipitation phase evolution. *Mater. Sci. Eng. A* **2018**, *731*, 577-582. doi.org/10.1016/j.msea.2018.06.094
73. Sherbinin, V.F.; Leonov, V.P.; Malinkina, Yu.Yu. Increase in corrosion resistance of titanium alloy in concentrated aqueous solutions of chlorides at high temperatures. *Inorg. Mater. Appl. Res.* **2013**, *4*, 537-541. doi:10.1134/S2075113313060117
74. Bokhonov, B.; Ukhina, A.; Dudina, D. et al. Carbon uptake during Spark Plasma Sintering: investigation through the analysis of the carbide "footprint" in a Ni-W alloy. *RSC Advances* **2015**, *5*, 80228-80237. doi:10.1039/C5RA15439A
75. Dudina, D.V.; Bokhonov, B.B.; Ukhina, A.V. et al. Reactivity of materials towards carbon of graphite foil during Spark Plasma Sintering: A case study using Ni-W powders. *Mater. Lett.* **2016**, *168*, 62-67. doi:10.1016/j.matlet.2016.01.018
76. Gornakova, A.S.; Straumal, B.B.; Prokofiev, S.I. Coarsening of (αTi) + (βTi) microstructure in the Ti-Al-V alloy at constant temperature. *Adv. Eng. Mater.* **2018**, *20*, 1800510. doi:10.1002/adem.201800510
77. Gornakova, A.S.; Prokofjev, S.I. Energetics of intergranular and Interphase boundaries in Ti-6Al-4V alloys. *J. Mater. Sci.* **2020**, *55*, 9225-9236. doi:10.1007/s10853-020-04432-w
78. Hein, K.; Buhrig, E. (Eds.) *Kristallisationaus Schmelzen*; VEB Deutscher Verlag für Grundstoffindustrie: E. Leipzig, Germany, 1983; 356 p. (in Germany).
79. Huang, S.; Zhang, J.; Ma, Y. et al. Influence of thermal treatment on element partitioning in α+β titanium alloy. *J. Alloys Compd.* **2019**, *791*, 575-585. doi:10.1016/j.jallcom.2019.03.332